Improving the Quality of Terrain Measurement

Hurtford Smith III

Thesis submitted to the faculty of the Virginia Polytechnic Institute and State University

in partial fulfillment of the requirements for the degree of

MASTER OF SCIENCE

in

Mechanical Engineering

John B. Ferris, Committee Chair

Steve Southward

Saied Taheri

Presented this 4th day of May in the year of our Lord 2009

Danville, Virginia

Keywords: measure, terrain profile, terrain surface, extraction, excitation, calibration

Improving the Quality of Terrain Measurement

Hurtford Smith III

Abstract

The emergence of high-fidelity vehicle and tire models has raised the requirements for terrain measurement capabilities. Inaccuracies that were once tolerable for measurement of general terrain roughness are no longer acceptable for these new applications. The techniques in this work seek to improve the quality of terrain measurement in addition to providing an objective way to describe the accuracy of these measurements. The first portion of this work develops an accuracy verification procedure for terrain measurement systems. This procedure involves a static test to assess the limitations of the profiler's laser height sensor, and a corresponding dynamic test to evaluate the limitations of the positioning sensors. Even with a well calibrated system, inertial errors will accumulate. The second portion of this work develops techniques to address these inertial errors in the data post-processing phase. A general correction technique is developed for any terrain type and a more computationally efficient technique is developed for smooth surfaces.

For basic ride and handling simulations, 3D terrain surfaces are computationally impractical, as the models used for these simulations only require point excitation. Current road profilers acquiring these 2D data use single-point lasers that capture localized disturbances that would be mechanically filtered by the tire and suspension in the physical vehicle system. The final chapter in this work develops a method to extract a 2D terrain profile from a 3D terrain surface. By considering all of the information in the tire contact patch, the filtering properties of the tire are approximately emulated.

Dedication

To my family and friends for their unwavering support…

Acknowledgements

I would like to begin by thanking God for the countless ways that He has blessed my life. To Him be the glory forever.

Thank you to the brave men and women that gallantly fight protecting our freedoms in this great nation. Without their sacrifice, I would never have been afforded the opportunity to pursue my dreams.

I would also like to extend my sincerest gratitude to Dr. John Ferris who has provided invaluable aid and advice throughout the course of this research. Thank you to my committee members, Dr. Said Taheri and Dr. Steve Southward, for offering their recommendations on my research and for teaching very beneficial classes.

Thank you to the all of the members of the VTPL. I am very fortunate to have been a part of such an excellent team. Specifically, thank you Zach for your companionship through a host of technical issues. Working beside you through the past two years was a pleasure.

Thank you IALR for providing technical and administrative support. This research would not have been possible without the incredible resources available at this facility.

Finally, I would like to thank Jessica for being a constant source of moral support.

Contents

List of Figures

List of Tables

1. Introduction

Terrain measurement systems began as simple 2D devices used by transportation departments to monitor road roughness [1-5]. As computer power increased and signal processing techniques evolved, 3D terrain measurement systems were developed [6, 7]. Typically, terrain measurement systems incorporate a scanning laser [8] that is rigidly mounted to the body of a host vehicle [6, 7, 9]. This vehicle traverses the terrain while simultaneously acquiring terrain measurements. When the vehicle encounters a disturbance, the laser oscillates with the body of the host vehicle. To obtain accurate terrain measurements, the motion of the vehicle must be accurately measured so that it can be rejected from the laser measurements.

In addition to pavement health monitoring, these high fidelity terrain surfaces are used as excitations to vehicle models to accurately predict the loading and responses of a physical vehicle. For instance, throughout a chassis development program it is necessary to possess load data representing severe customer usage to ensure that the chassis will perform as required. Unfortunately, actual loads are only available at the conclusion of the program. The design engineer is challenged with using predicted chassis loads early in the design process, when changes are relatively easy and inexpensive to make and measured chassis loads much later in the program. Once the measured loads become available, design changes are extremely costly if allowed to be implemented at all. Similar difficulties are faced by tire engineers since tractive efforts are largely dictated by the tire-terrain interaction site [10]. It is advantageous, therefore, to accurately predict these target loads early in the development program and to maintain a consistent process for predicting loads as the design changes throughout the program [11-13].

Current 3D terrain measurement systems acquire approximately one million data points per second [8]. This data acquisition rate improves the available signal bandwidth and allows sharp disturbances to be detected in both the lateral and longitudinal directions. Capturing these disturbances is critical; the driver's perception of ride quality

is largely dictated by these events [14] and chassis durability is highly sensitive to transient loading [15]. For longer stretches of terrain, storing and manipulating these data is a daunting task [16]. One benefit of the techniques developed in this work is a reduction in the data required to represent the measured terrain topology. This representation issue must also be considered in terms of tire interaction with the terrain. Accurate vehicle simulation requires consideration of tire bridging and envelopment, in which the vehicle responses will not be affected by narrow cracks and small stones in the terrain surface [2, 17]. The specific novel contributions of this work are the following:

1) A comprehensive accuracy test for high-fidelity terrain measurement systems
2) Two application-specific methods for attenuating inertial errors in terrain data
3) A method to extract a 2D terrain profile from a 3D terrain surface that emulates a tire's mechanical filtering properties

This work documents recent developments in terrain measurement for vehicular simulations and pavement health monitoring. Throughout the course of this work, a terrain profile is defined as a longitudinal measurement in 2D and a terrain surface is defined as a 3D terrain measurement. The remainder of this work is developed as follows. Chapter 2 presents the evolution and developments in terrain measurement leading up to this work. Chapter 3 develops techniques for calibrating terrain measurement systems. This technique involves exciting the host vehicle at its first two resonant frequencies while simultaneously measuring a machined calibration surface. Even with a well calibrated terrain measurement system, cumulative inertial errors develop due to equipment drift. Chapter 4 develops post-processing techniques to address this equipment drift in the data post-processing phase. This work concludes by developing a technique for mapping a 2D profile from a 3D terrain surface. 3D terrain surfaces capture terrain characteristics more effectively than 2D terrain profiles; however, the copious data produced by these systems render them impractical for examining long stretches of terrain. Chapter 5 develops a method that incorporates information from a 3D surface into a 2D profile.

2. Background

2.1 2D Terrain Profile Measurement

The technology developed to measure terrain has progressed from vehicle-response systems [18, 19] to the measurement of various types of terrain using vehicle-independent systems [6, 7, 9, 20]. Vehicle-response systems estimate the terrain surface based on vehicle responses such as spindle accelerations and loads. The accuracy of the resulting effective terrain profile relies on the fidelity of the vehicle and tire models. There are numerous modeling difficulties in this process (e.g., the enveloping property of tires precludes capturing the sharpness of terrain events); therefore, vehicle-response measurements should only be used to describe the terrain's influence on the host vehicle or making general statements about terrain roughness.

A better method is direct measurement of terrain. General Motors Research (GMR) developed a high-speed inertial profiler in the 1960s [21]. This profiler uses a rigid road-following wheel that extends below the body of either a vehicle or trailer to measure the relative distance between the body and the road surface. An accelerometer is attached to the body and, having integrated the signal twice, measures the absolute vertical position of the body. The resulting road profile is the difference in the signals.

In 1987, The Australian Road Research Board (ARRB) substituted a laser for the road-following wheel [22]. In this system, the terrain is sampled optically, rather than mechanically as had been the standard practice. Although advances were made because of this fundamental change, considerable research is required to understand the implications of this shift. For example, the laser has a much finer resolution than the tire contact patch. This fine resolution fundamentally differs from that of a tire. The lasers are capable of detecting small localized disturbances that would be enveloped or bridged by the tire of a typical passenger vehicle [23]; this problem had not surfaced previously because the tire acted as a mechanical filter between the terrain surface and vehicle chassis.

2.2 3D Terrain Surface Measurement

Recent optical and computational advances have produced pavement profiling scanners [8] which can obtain millimeter precision across a wide transverse path. These 3D scanners are capable of differentiating between small localized disturbances and disturbances that will excite the vehicle chassis, but validating the accuracy of these surfaces is an ongoing research subject [24]. This problem is exacerbated by the fact few of these systems currently exist, limiting the availability of data.

3D terrain surface measurement systems consist of a scanning laser and some combination of an inertial navigation system (INS), accelerometers, a distance measurement instrument, and inclinometers to track the position and orientation of the scanning laser in space. The Vehicle Terrain Measurement System (VTMS) used to acquire data for this work can be seen in Figure 2-1. The scanning laser is rigidly mounted at the rear of the vehicle. Each transverse scan consists of 940 measured points across a 4m width [6, 7].

Figure 2-1: Vehicle Terrain Measurement System

The precision of the VTMS is summarized in Figure 2-2. For short distances (i.e., less than 1 meter) the precision of the system is limited by the spot size of the laser at 1

mm [6]. As the distance traveled by the VTMS extends into the kilometer range, the precision is limited by the INS system. When all the GPS signals are being collected (i.e., there is a sufficient number of satellites that can be observed), then the INS system is capable of 2 centimeter placement accuracy. For instances in which the base station is not available, the rover GPS is capable of using a correction service for sub-meter to decimeter level accuracies. In the worst case scenario, the INS system can obtain 0.8-1.2 meter accuracy using the standard L1/L2 band GPS frequencies [25].

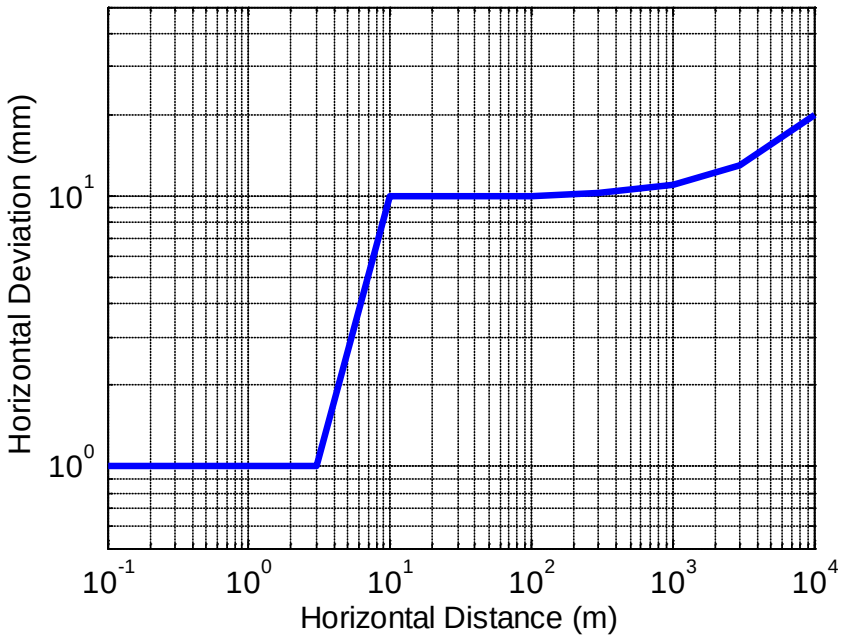

Figure 2-2: Horizontal Precision of the VTMS

The 3D scanning laser on the VTMS collects data transversely through the application of a rotating prism [8, 26, 27]. Figure 2-3 illustrates how the scanning laser acquires a single transverse scan. The data are collected at equal angles of rotation, shown as θ in Figure 3.1. When a flat surface is being scanned, the transverse spacing between measurement points is closer at the center of the scan than at the edges of the scan. This issue is exacerbated when there are local disturbances in the surface being measured. Figure 2-3 illustrates the transverse spacing locations for such a surface, shown as x_1, x_2, and x_3. Due to the undulations in the surface, transverse spacing between points x_1 and x_2 is significantly less than the spacing between points x_2 and x_3. In the longitudinal direction, the spacing is controlled by speed of the host vehicle and, to a

lesser degree, the yaw and pitch rates. Consider, for example, a host vehicle velocity of 5 m/s. The laser acquires 1,000 scans every second, which in this example equates to 200 scans/m or 1 scan every 5 mm.

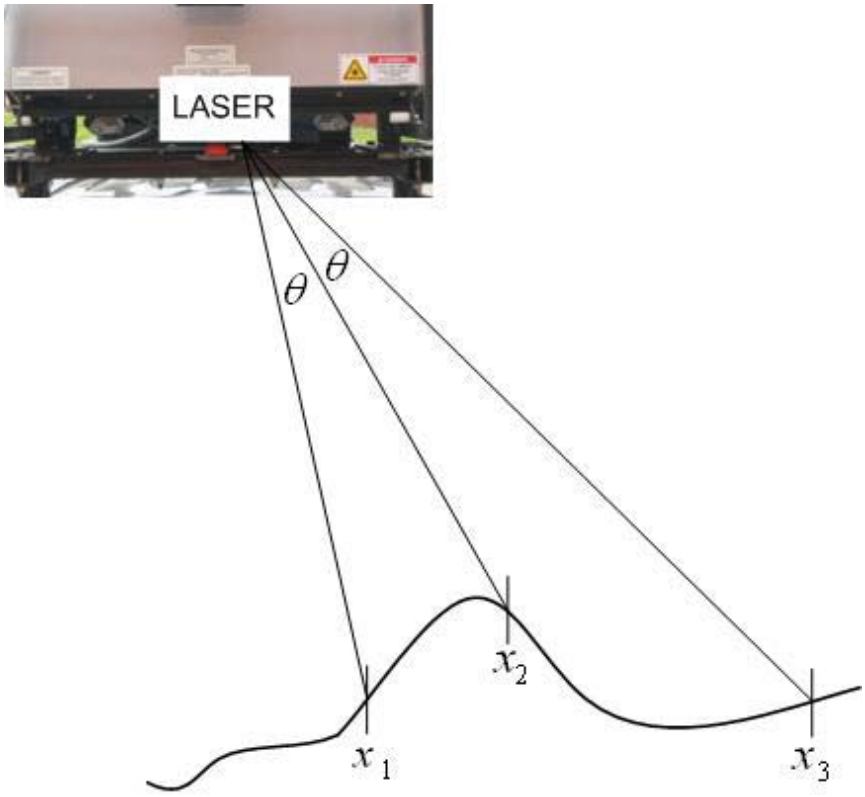

Figure 2-3: Schematic of Consecutive Non-Uniformly Spaced Laser Samples

2.3 Removing Host Vehicle Body Motion from Laser Measurements

As a vehicle travels over terrain, it experiences bumps and dips which cause the absolute height of the vehicle to be constantly changing with time. The scanning laser on terrain profilers is rigidly mounted to the host vehicle and consequently, the laser position and orientation also changes with time. In this way, the motion of the vehicle is convolved with the motion of the terrain in the laser measurements. The motion of the laser must be rejected from the laser measurements to obtain the actual terrain profile. If this motion is not subtracted, the data is inaccurate and the simulated vehicle over the measured terrain experiences loads very different from the actual forces experienced by the physical vehicle over the actual terrain.

To characterize the laser's motion through space and time, the VTMS uses an INS augmented by three coplanar accelerometers. Figure 2-4 is an overview of the data-acquisition systems on the VTMS. First, consider the INS path, which is labeled 1) in the figure. The INS consists of a rover GPS antenna, a base station GPS antenna, and an inertial measurement unit (IMU). The rover data are corrected with the base station data via the differential GPS correction process and then combined with the IMU data in a Kalman filter. All of the INS processing to this point is done in commercially available software. The INS data are then low passed filtered at 10 Hz to provide the first estimate of the laser's position and orientation in space and time. Three coplanar accelerometers, in the path labeled 2) in the figure, are used to describe planar laser motions such as pitch and roll. The accelerometer data are high-pass filtered at 10 Hz and then integrated twice to produce the second estimate of the laser's position.

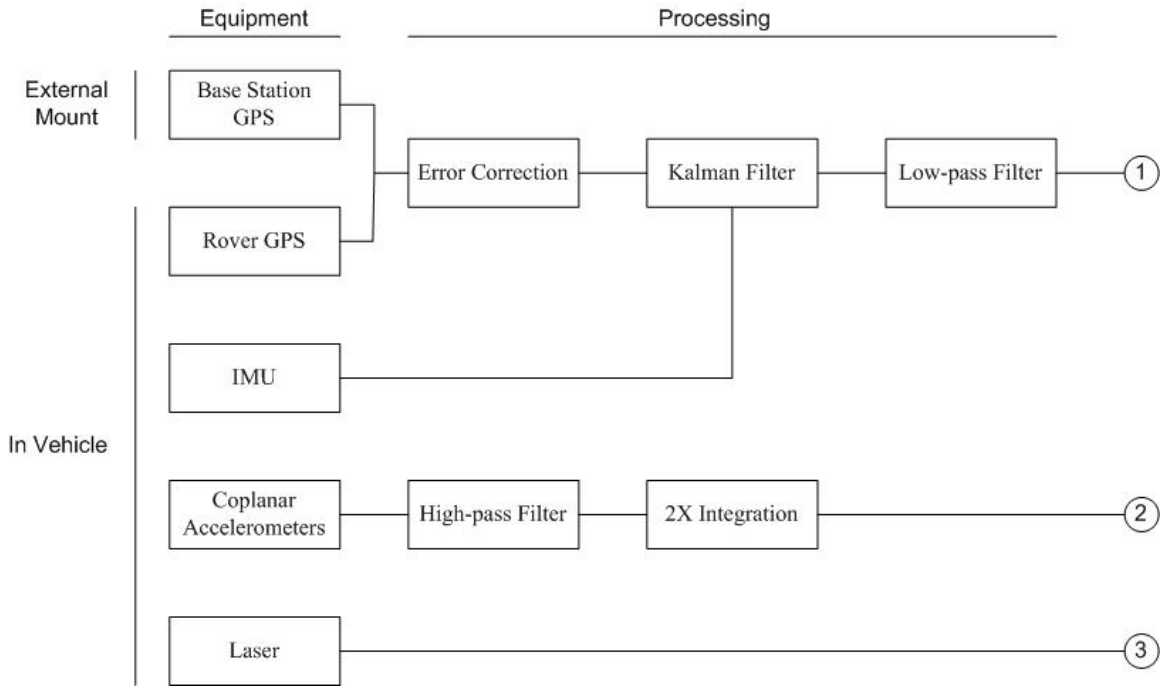

Figure 2-4: VTMS Hardware and Data Acquisition Overview

Before the motion data are subtracted from the laser, a common coordinate system is established. The lever arm offset between the rover antenna and the IMU, and the offset between laser and the IMU are inputs into the commercial INS post processing

software so that the output position file is body centered about the laser. Additionally, the accelerometer's coordinate system is translated to the laser. Once all of the sensor data has a common coordinate system and the data are synchronized in time [7], the motion information is subtracted from the laser data.

To maximize the usefulness of the post-processed terrain information, a space 3/123 coordinate transformation assigns each measured data point a location relative to the base station antenna of the INS. Equation (2-1) is the space 3/123 rotation matrix, where ω, φ, and κ are the Euler angles for roll, pitch, and yaw respectively. The global coordinates are defined such that the horizontal and vertical coordinates have their positive sense in the Easting and Northing directions, respectively.

$$\begin{bmatrix} \cos(\phi)\cos(\kappa) & \cos(\omega)\sin(\kappa)+\sin(\omega)\sin(\phi)\cos(\kappa) & \sin(\omega)\sin(\kappa)-\cos(\omega)\sin(\phi)\cos(\kappa) \\ -\cos(\phi)\sin(\kappa) & \cos(\omega)\cos(\kappa)-\sin(\omega)\sin(\phi)\sin(\kappa) & \sin(\omega)\cos(\kappa)+\cos(\omega)\sin(\phi)\sin(\kappa) \\ \sin(\phi) & -\sin(\omega)\cos(\phi) & \cos(\omega)\cos(\phi) \end{bmatrix} \quad (2\text{-}1)$$

Consider the digital photograph and the two terrain renderings of a sidewalk and curb seen in Figure 2-5. The photograph labeled (a) corresponds with the two renderings labeled (b) and (c). For this run, the rear wheels of the VTMS were backed up onto the sidewalk and then the vehicle was driven off the curb. Rendering (b) maps the terrain surface before the common mode of laser oscillation has been appropriately rejected from the laser measurements. Notice the large wave on the sidewalk occurs right as the vehicle's wheels fall off of the curb. Rendering (b) is the same run of terrain data; however, the common mode of laser oscillation has been appropriately rejected using the information from the INS and the accelerometers [6, 7].

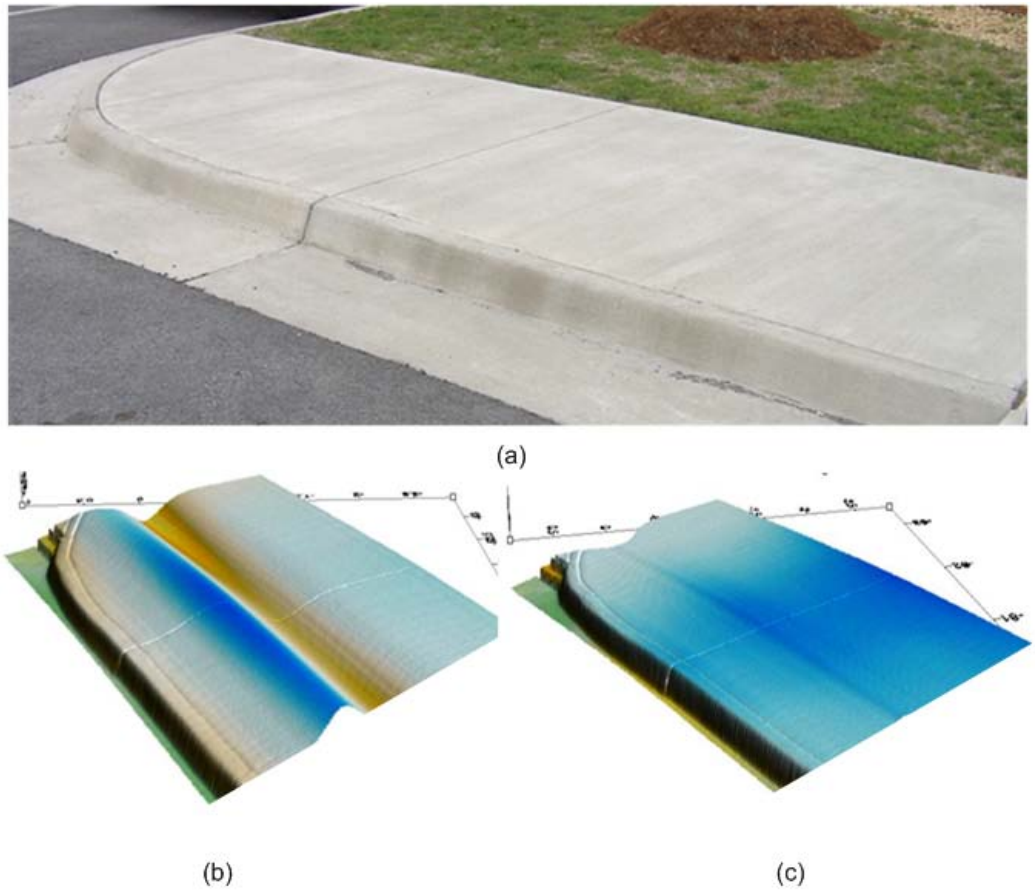

Figure 2-5: Body Motion Problem

The assumption that the sprung mass of a vehicle is a rigid body may be reasonable for many applications; however, when millimeter accuracy is desired from a terrain profile, this assumption may not be valid. The IMU is, therefore, mounted as closely and rigidly to the laser as possible. Rigid mounting guarantees the rotations experienced by the IMU are the same as those experienced by the laser. In addition, this configuration allows a simple kinematic relationship to be developed that describes the laser motion with respect to the IMU motion (both rotations and translations). The high sample rate of the A/D converter for the accelerometers makes them appropriate to remove high frequency motion. The accelerometers are rigidly mounted as close to the scanning laser as possible. Figure 2-6 shows the accelerometers (upper image, indicated by arrows) mounted immediately under the laser system and the IMU location (Figure 2-6, lower image).

Figure 2-6: Measurement Hardware Mounted at Scanning Laser

3. Calibrating Terrain Measurement Systems

3.1 Chapter 3 Introduction

One major difficulty in measuring terrain profiles is assessing the accuracy of the measurement. Many Department of Transportation agencies certify terrain profilers by having vendors measure a specified road segment and then comparing the resultant measurements to some reference profile [2, 3, 28-31]. These reference profiles are acquired using a rod and level [32] or other laser-based devices [2, 33]. This comparison strategy evaluates the overall profiling system (equipment, manufacturers, processes, and technicians measuring the test sites). These system-level testing processes effectively evaluate a terrain profiler's ability to produce repeatable measurements. While this procedure is necessary in determining the comparative value of a particular profiling system, system-level testing is not sufficient to answer the seminal question of accuracy: how accurately does a piece of equipment measure the terrain profile? In this work, the measured profile is compared to a machined surface.

Two subsystems must be evaluated to fully assess the accuracy of a terrain profiler. First, the sensor that measures relative height must be evaluated (in most modern systems, this sensor is a noncontact optical device). Next, the profiler's positioning system must be properly evaluated. The positioning system must be able to repeatedly measure longitudinal distance [2] and remove the vehicle body motion in the processed data files.

While it is critical to assess the laser's ability to measure the relative distance from itself to the terrain, this performance metric alone produces an unreasonably optimistic estimate of the accuracy with regard to vehicle movement. By exciting the vehicle at its resonant frequencies, high amplitude vibration is induced that tests the terrain profiler's ability to remove severe laser motion in the processed data files [5]. Additionally, the laser measurement system's ability must be confirmed by measuring sharp edged (high bandwidth) events. The calibration surface also must be simple, light, and reproducible to ensure that it is convenient to use.

This chapter proposes to design an excitation event (that will excite the host vehicle at its primary ride and wheel-hop frequencies) and a calibration surface to objectively highlight the capabilities and inadequacies of a terrain profiler. The data acquired on a terrain profiler are combined in post-processing to remove the vehicle body motion of the terrain profiler at these resonant frequencies. If the system successfully removes body motion under these adverse conditions, it is assumed that the system will remove body motion under more favorable conditions. The remainder of this chapter is developed as follows. First, the geometric design requirements of an excitation event are developed that will excite the terrain profiler at its first two resonant frequencies. Next, the design requirements for a calibration surface are developed. An experimental testing procedure is developed that systematically evaluates each component of the terrain measurement system. Finally, a design example is presented that evaluates the terrain profiler in Figure 2-1.

3.2 Chapter 3 Background

The Federal Highway Administration (FHWA) and many state agencies have adopted the International Roughness Index (IRI) as the primary method by which to monitor road surface roughness [2, 5, 34, 35]. This simple composite roughness statistic is calculated using a quarter car vehicle model, as seen in Figure 3-1, with a fixed set of parameters called the Golden Quarter Car model [35]. The quarter car model is also used to predict basic vehicle ride characteristics (for this work, the primary ride and wheel-hop frequencies). Table 1 in the Appendix lists the parameters associated with the quarter car model in Figure 3-1.

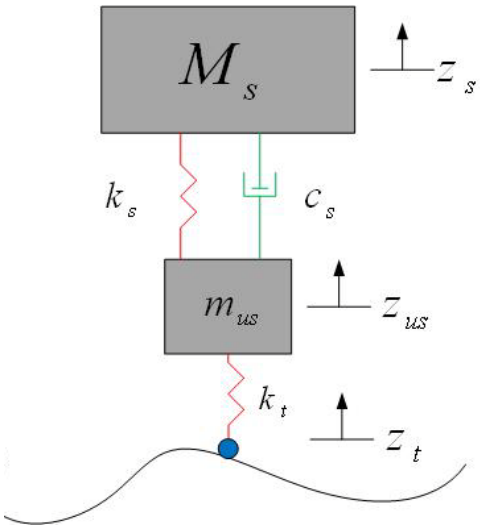

Figure 3-1: Quarter car model

This two degree of freedom model has two resonant frequencies: the primary and secondary (or 'wheel-hop') ride frequency. While an actual vehicle contains many degrees of freedom and resonant frequencies, the quarter car model approximates the two ride modes typically encountered under normal driving conditions. The quarter car has been shown by Sayers to accurately estimate automobile ride quality [36]. The free body diagrams of the two masses yield the following equations of motion [37]:

$$M_s\ddot{z}_s + c_s\dot{z}_s - c_s\dot{z}_{us} + k_s z_s - k_s z_{us} = 0 \tag{3-1}$$

$$m_{us}\ddot{z}_{us} + c_s\dot{z}_{us} + (k_s + k_t)z_{us} - k_s z_s = k_t z_t \tag{3-2}$$

Rewriting these equations in matrix form:

$$\begin{bmatrix} \ddot{z}_s \\ \ddot{z}_{us} \end{bmatrix} = \begin{bmatrix} -\frac{c_s}{M_s} & \frac{c_s}{M_s} \\ \frac{c_s}{m_{us}} & -\frac{c_s}{m_{us}} \end{bmatrix} \begin{bmatrix} \dot{z}_s \\ \dot{z}_{us} \end{bmatrix} + \begin{bmatrix} -\frac{k_s}{M_s} & \frac{k_s}{M_s} \\ \frac{k_s}{m_{us}} & -\frac{(k_s + k_{us})}{m_{us}} \end{bmatrix} \begin{bmatrix} z_s \\ z_{us} \end{bmatrix} + \begin{bmatrix} 0 \\ \frac{k_{us}}{m_{us}} \end{bmatrix} z_t \tag{3-3}$$

The two eigenvalues generated by the mass normalized stiffness matrix produce the primary and secondary ride frequencies [38]. Determining these frequencies will drive the design of an excitation event that excites the vehicle at these frequencies.

3.3 Designing an Excitation Event

The objective of this section is to design a controlled excitation event that evaluates profilers under adverse measurement conditions. The design of an appropriate excitation event depends on the ride dynamics of the terrain measurement system; that is, the excitation event must include both the primary and secondary ride frequencies of the terrain measurement system. An indication of how well a given terrain profiler measures sharp transitions is also required since sharp transitions are a critical factor in chassis durability [15] and the perception of ride quality [14]. The excitation event must also be easy to build and transport or it simply will not be used, as is the case with more complicated designs that have been proposed [35]. Figure 3-2 is a general excitation event schematic, where a is the cleat spacing, w is the width of the cleat, and $L_{excitation}$ is the longitudinal length of the excitation event. A complete list of excitation event parameters is found in Table 2 in the Appendix.

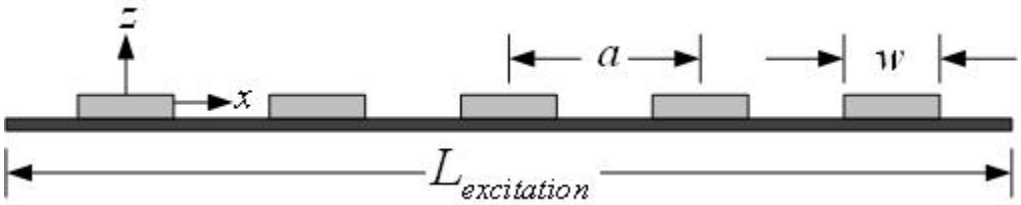

Figure 3-2: Schematic of excitation event oriented longitudinally

The length of the excitation event, $L_{excitation}$, and the velocity at which the terrain profiler travels, V, are determined such that primary ride motion is excited. Therefore, the length of the excitation event must be equal to half of the wavelength corresponding to the primary ride frequency. Of course this wavelength is also a function of the terrain profiler velocity; this relationship is shown graphically in Figure 3-3 and written explicitly in Equation (3-4). It is clear that either the terrain profiler speed or the length of the excitation event is an available design parameter; either can be chosen and the relationship defined by Equation (3-4) can be satisfied. The length of the excitation event must be a reasonable size and, preferably, made from inexpensive materials. The length of the excitation event is chosen to be 2.44 meters (8 feet) so that a typical sheet of plywood can be used. The terrain measurement system's velocity is determined from

Equation (3-4) given the primary ride frequency in Hz and the length of the excitation event.

$$V = 2L_{excitation} f_1 \tag{3-4}$$

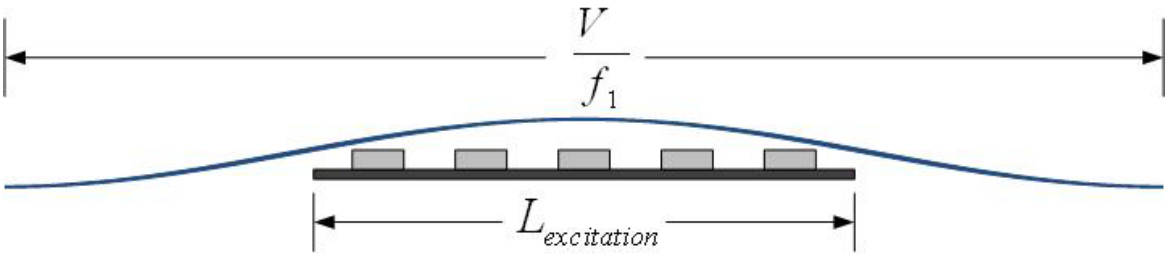

Figure 3-3: Excitation Event Length

The spacing of the cleats, *a*, is designed such that the secondary ride frequency is excited. The spacing of the cleats must correspond to one complete wavelength of the secondary ride frequency. Again, this wavelength is a function of the terrain profiler velocity that is prescribed by Equation (3-4) ; this relationship is shown graphically in Figure 3-4 and written explicitly in Equation (3-5).

$$V = af_2 \tag{3-5}$$

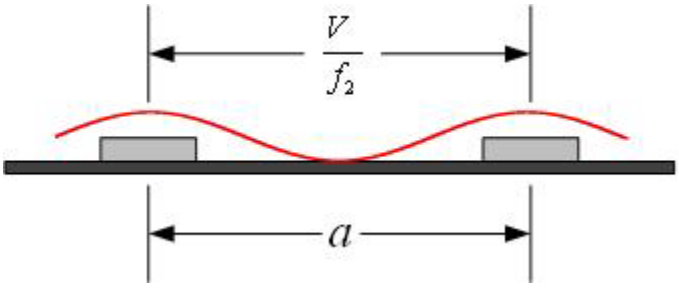

Figure 3-4: Excitation Event Cleat Spacing

The cleat spacing is determined from Equation (3-5) given the terrain profiler velocity and the secondary ride frequency. The secondary ride frequency is more difficult to estimate than the primary ride frequency and a simpler method to determine the cleat spacing may be required. As an alternative formulation, Equation (3-4) and Equation (3-5) can be combined so that the cleat spacing is calculated directly from the

ratio of the first two natural frequencies and the prescribed length of the excitation event. The ratio of the primary ride and wheel-hop frequencies of a typical passenger vehicle is approximately 1:10 [17]. Equation (3-6) is simplified by exploiting this typical ratio. Therefore, when the host vehicle is a typical passenger car, there should be five evenly spaced cleats per excitation event.

$$a = 2L_{excitation}\left(\frac{f_1}{f_2}\right) = \frac{L_{excitation}}{5} \tag{3-6}$$

Finally, the width and height of the individual cleats must be determined. Recall that the cleat spacing is designed to excite the wheel-hop frequency. This mode is approximated by a single degree-of-freedom oscillator (i.e., the movement of the vehicle body is negligible). When an underdamped, single degree-of-freedom, oscillator is sinusoidally excited, the displacement transmissibility ratio, *T*, is defined in Equation (3-7) [38].

$$T = \left[\frac{1+(2\zeta_s r)^2}{\left(1-r^2\right)^2+(2\zeta_s r)^2}\right]^{\frac{1}{2}} \tag{3-7}$$

Where *r* is the frequency ratio and ζ_s is the suspension damping ratio. At resonance, the frequency ratio is $r = \sqrt{1-2\zeta_s^2}$ [38] and Equation (3-8) simplifies to

$$T^2 = \frac{1+4\zeta_s^2-8\zeta_s^4}{4\zeta_s^2\left(1-\zeta_s^2\right)} \tag{3-8}$$

In the case of a rectangular cleat, the amplitude of the excitation is half of the height of the cleat and the damping ratio corresponds to the damping ratio for the secondary ride mode. One objective of this chapter is to design an event that excites the secondary ride mode. In order to best excite this response, the width of the cleat should be dimensioned such that the point *P* (shown in Figure 3-5) lies along the line of oscillation (shown as a red line).

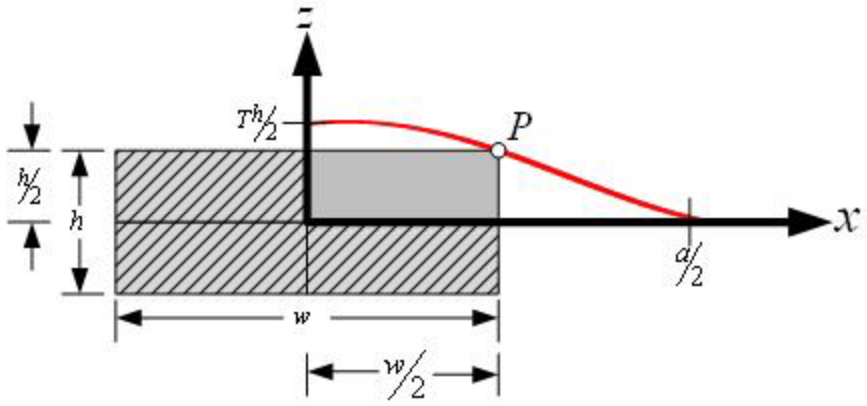

Figure 3-5: Single degree of freedom oscillator over cleats

The equation for damped sinusoidal oscillation is given by Equation (3-9), where A is the response amplitude and $\omega_2 = 2\pi f_2 \sqrt{1-\zeta_s^2}$.

$$z(t) = A\cos(\omega_2 t) \tag{3-9}$$

Using Equation (3-8) with an excitation amplitude of *h/2* Equation (3-9) becomes Equation (3-10).

$$z(t) = \frac{h}{2} T \cos\left(2\pi f_2 \sqrt{1-\zeta_s^2}\, t\right) \tag{3-10}$$

Substituting Equation (3-5) into Equation (3-10) produces Equation (3-11).

$$z(t) = \frac{h}{2} T \cos\left(\frac{2\pi V \sqrt{1-\zeta_s^2}\, t}{a}\right) \tag{3-11}$$

At point P, a longitudinal distance constraint, *Vt=w/2*, and a height constraint, *z=h/2*, is imposed resulting in Equation (3-12).

$$\frac{h}{2} T \cos\left(\frac{w\pi\sqrt{1-\zeta_s^2}}{a}\right) = \frac{h}{2} \tag{3-12}$$

Equation (3-12) is rewritten in terms of the cleat width, *w*, and given in Equation (3-13).

$$w = \frac{\cos^{-1}\left(1/T\right)}{\pi\sqrt{1-\zeta_s^2}}a \tag{3-13}$$

Note that the width of the cleat, *w*, is only a function of the damping ratio of the secondary ride mode and the cleat spacing. The height of the cleat, *h*, is left to be determined. Setting the height at 38 millimeters (1.5 inches) allows a standard lumber size to be used and is thus done for the remainder of this chapter. Figure 3-6 plots the ratio *w/a* as a function of the damping ratio, ζ_s.

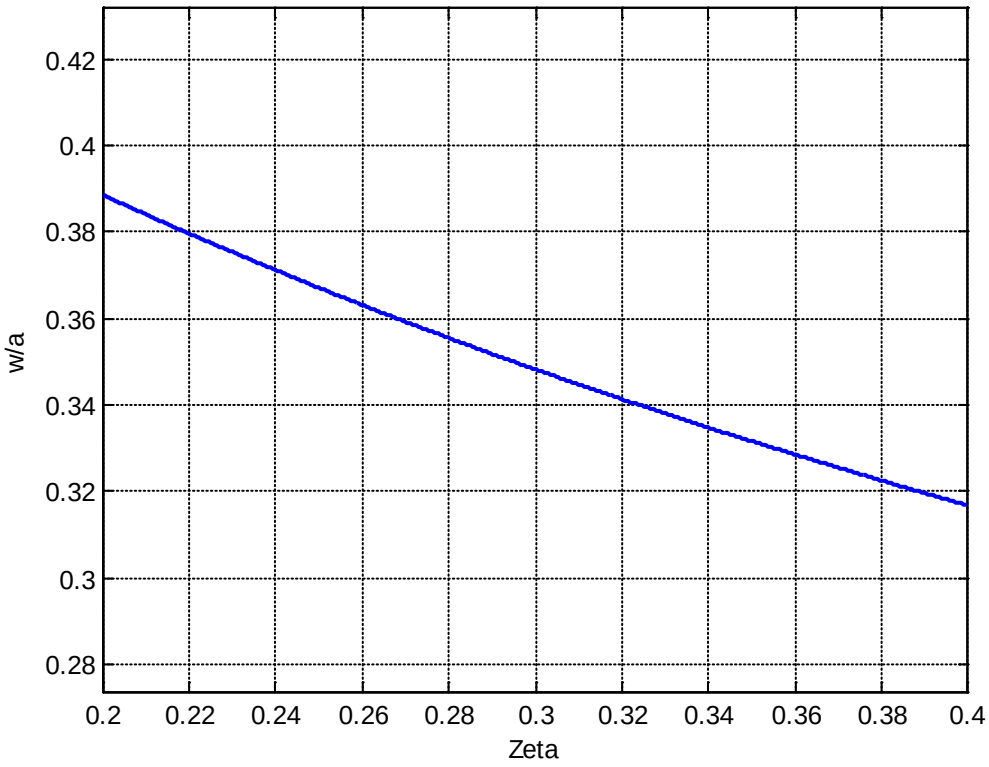

Figure 3-6: The Ratio w/a versus Zeta

Assuming a damping ratio of $\zeta_s = 0.3$, Equation (3-13) reduces to Equation (3-14).

$$w = 0.35a \tag{3-14}$$

These results are very favorable; all the design criteria can be met using inexpensive, readily available materials.

3.3.1 Obtaining Vehicle Parameters

To increase the accuracy of the process, the vehicle's ride frequencies are physically measured. This may prove to be particularly important if the host vehicle contains several hundred pounds of equipment, as is the case of the VTMS in Figure 2-1. To accurately measure these frequencies, the vehicle is instrumented with accelerometers at each of the four wheel spindles and tested on the Virginia Institute for Performance Engineering and Research (VIPER) eight post shaker rig as seen in Figure 3-7.

Figure 3-7: VTMS on VIPER Shaker Rig

The shaker rig consists of four hydraulic actuators that provide the vehicle excitations. For the purpose of this test, the actuators executed a sinusoidal sweep in "heave" (all four actuators moving in unison) mode. Each test run on the shaker rig consisted of a constant velocity input of varying frequency. The data used to extract the primary and wheel hop frequencies came from two run types. The first run consisted of a frequency sweep from 1-30 Hz with a maximum actuator velocity of 152.4 mm/s and the second run consisted of a sweep from 6-30 Hz with a maximum actuator velocity of 254 mm/s. To extract the primary ride and wheel hop frequencies, the accelerometer data are numerically integrated to obtain velocity data and then the power spectral density (PSD) of the data are analyzed. The PSD of the velocity data from the right-front corner, for the 1-30 Hz run, is shown in Figure 3-8.

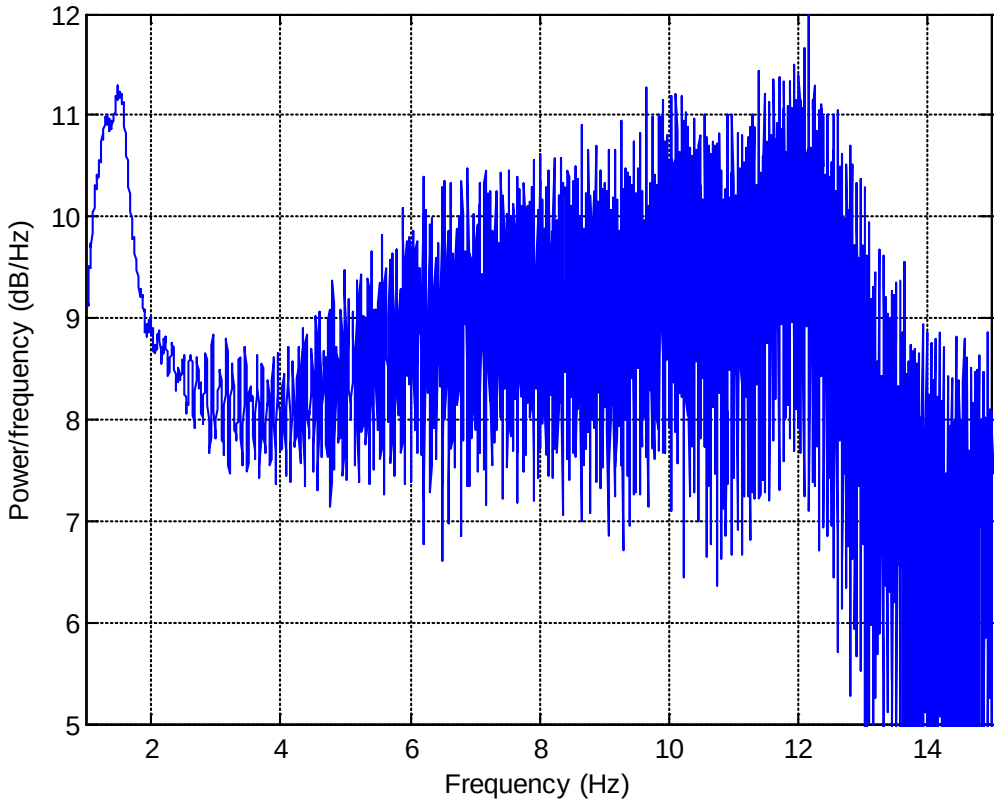

Figure 3-8: PSD for the Velocity Signal at Corner 2 for the 1-30Hz Sweep

For a mechanical system, the highest power is seen at a system's resonant frequencies. In Figure 3-8, the first peak (which corresponds to the primary ride frequency) can clearly be seen at approximately 1.2 Hz; however, with such a low excitation amplitude at higher frequencies, the suspension is not seeing sufficient excitation to reliably identify a second resonant peak. Figure 3-9 plots the PSD from the same corner as in Figure 3-8 for 6-30 Hz run with a higher excitation velocity (and thus larger excitation amplitude at higher frequencies). Since the sweep begins at 6 Hz, the primary ride frequency cannot be extracted; however, the higher excitation velocity provides a more reliable picture of the location of the wheel-hop resonant frequency. Since this frequency is heavily damped, the wheel-hop resonant peak is not as apparent as the primary ride peak. From Figure 3-9, the wheel-hop frequency is somewhere in the range from 10-12 Hertz. Above about 12 Hertz, both plots exhibit excessive noise that is attributed to a highly nonlinear system response. Most of the noise arises from stiction in the dampers. Since the system is excited at a constant velocity, the amplitude in the higher frequency range is very small and thus suspension travel is low.

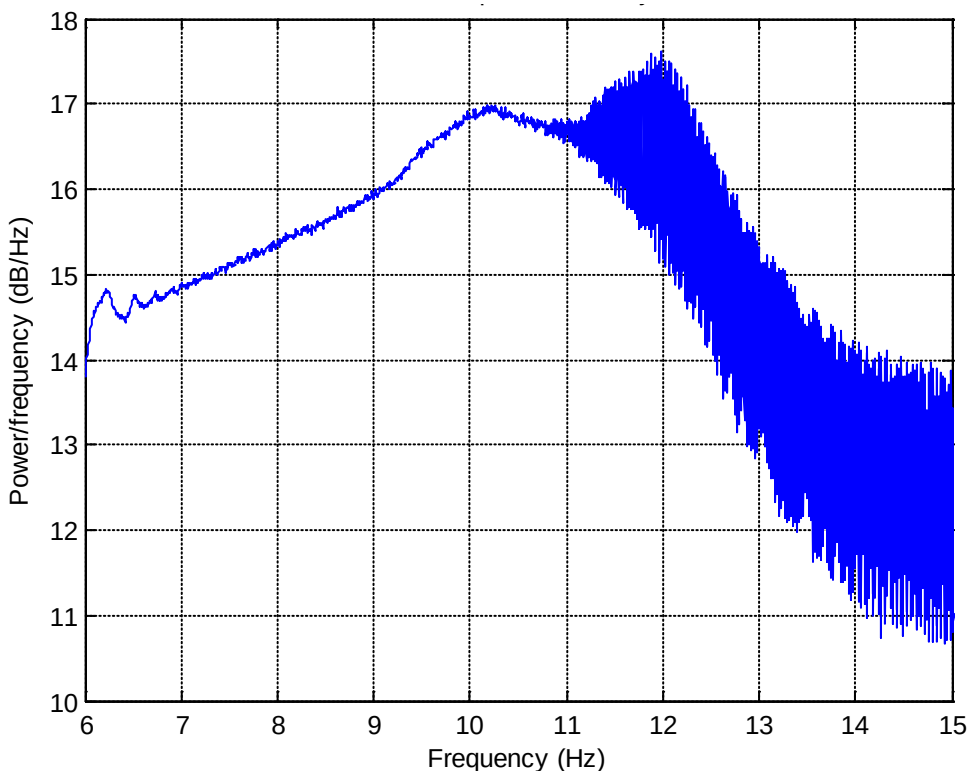

Figure 3-9: PSD for Velocity Signal at Corner 2 for the 6-30 Hz Sweep

3.3.2 Obtaining Excitation Event Parameters

Using Equation (3-6), the cleat spacing is calculated based on the first two ride frequencies (f_1, f_2) and the length of the excitation event (assumed to be 2.44 meters or 8 feet). Since the ratio of the ride frequencies is 1:10, within the measurement error, then Equation (3-6) is used to deduce the cleat spacing.

$$a = 2L_{Excitation}\left(\frac{f_1}{f_2}\right) = 2(2.44m)\left(\frac{1.1Hz}{11Hz}\right) = 0.49m(1.61ft) \tag{3-15}$$

Using Figure 3-6, the ratio *w/a* is determined to be 0.35 for a damping ratio of 0.3 [39]. Using *a* found in Equation (3-15), *w* is 0.17 meters (0.56 feet). Equation (3-5) calculates the host vehicle velocity based on the cleat spacing and the wheel-hop frequency. Substituting values from this example produces Equation (3-16).

$$V = af_2 = (1.86\,ft)(10.3Hz) = 19\,{}^{ft}\!/_{s}\,(5.79m/s) \tag{3-16}$$

Sample excitation events (one for each vehicle wheel path) are seen in Figure 3-10 and Figure 3-11 is a PSD plot of the VTMS's vertical acceleration traversing this event. The two peaks are within the error margin of the vehicle's primary ride and wheel-hop frequencies.

Figure 3-10: Sample Excitation Events

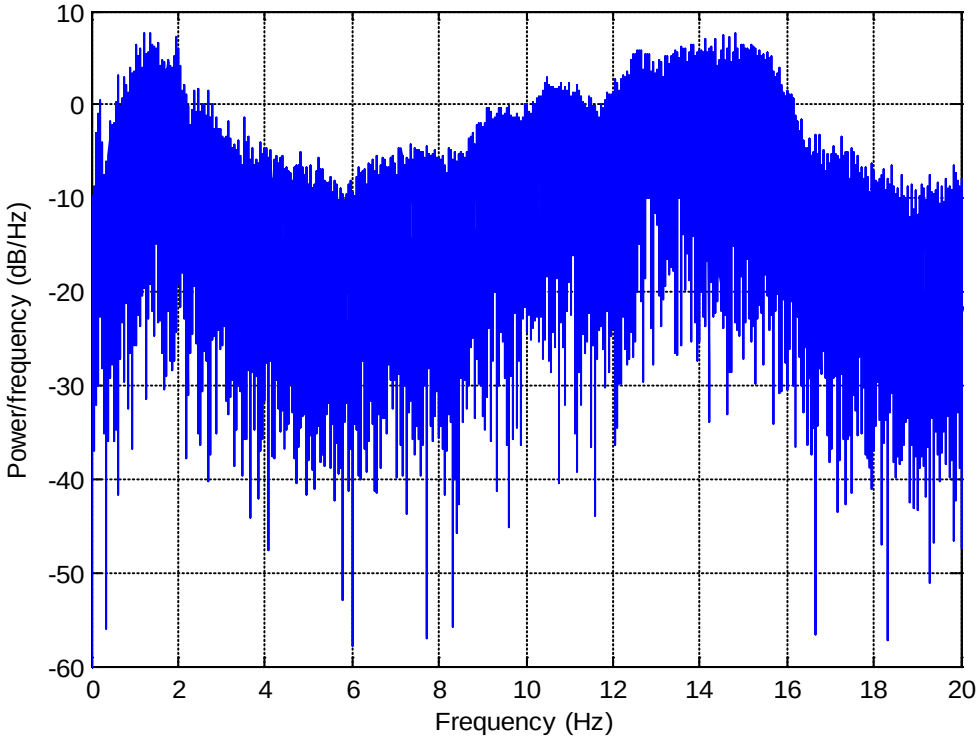

Figure 3-11: PSD of Vehicle's Vertical Acceleration

3.4 Designing a Calibration Surface

All terrain measurement systems include two primary subsystems. The first subsystem uses a sensor (typically optical) to measure the relative height between itself and the terrain surface. The second subsystem determines the height sensor's position and orientation. To properly evaluate the capabilities and limitations of a particular terrain measurement system, these subsystems must be evaluated for their ability to track the motion of the laser through space and time. Separate subsystem evaluation determines the maximum potential of each sensor; whereas, complete system evaluation will test sensor fusion and post-processing techniques (e.g., signal synchronization). To satisfy these criteria, a calibration surface is designed to meet four specifications:

1) The calibration surface must include sharp-edged high-bandwidth events. This specification is intended to evaluate the relative height measurement sensor. Sharp-edged transient events have been shown to be the most influential factor in the human perception of ride quality [14, 40]. If the laser is able to capture these transient events, it demonstrates that the sensor bandwidth is adequate.
2) The system must be insensitive to the reflectivity of the calibration surface. This specification is intended to evaluate the relative height measurement sensor. Most modern height sensors are laser-based measurement units. The laser height sensors must be able to automatically adjust internal gains to account for abrupt surface reflectivity changes that are encountered in typical operating environments (e.g., the painted lines on highways).
3) The profile of the calibration surface must be known to a high tolerance. This specification is intended to evaluate the ability of the position sensors to track the location of the laser as it moves through space and time when the vehicle is experiencing high-amplitude vibration. The profile of the calibration surface must be machined so that it exceeds the highest attainable resolution of the height sensor. Smith [24] proposes a method for constructing excitation events that will excite the host vehicles at its primary-ride and wheel-hop frequencies (see Section 3.3). These excitation events can then be mated with the calibration surface to

determine how effectively the data from the position sensors can be combined with the laser data to remove the host vehicle's body motion.

4) The calibration surface must be easily transported. While seemingly trivial, this specification is intended to make sure that the calibration surface is used frequently. Since the calibration surface must be machined, it is recommended that aluminum be the primary material so that portability is maintained.

Before the calibration surface can be properly constructed, the designer must have a thorough understanding of the sensors to be evaluated. The scanning laser on the VTMS measures the relative height between itself and the terrain using a phase modulation scheme [8, 26, 27]. A diode emits a laser that contacts a spinning mirror polygon where it is dispersed at equal angles transversely across the width vehicle. A schematic for the laser's scanning range is displayed in Figure 3-12.

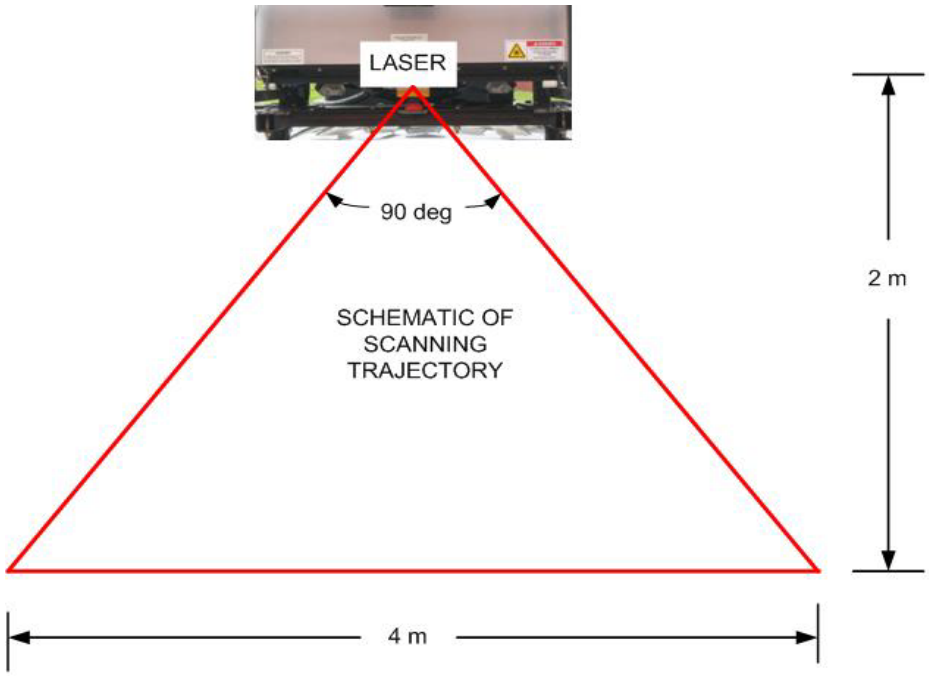

Figure 3-12: Scanning Laser Range Schematic

This measurement technique has an inherent limitation on the transverse slope that it is capable of measuring. This concept is illustrated in Figure 3-13. The laser is attempting to measure the sharp disturbance; however, it is incapable of measuring the red dotted line due to a shadowing effect. Figure 3-14 is a plot of the scan location

versus the maximum measurable slope limitation. At the center of the scan, the laser can nearly measure a 90 degree discontinuity. Scanning location "0" corresponds to the left side of the scan and location "4 m" refers to the right side of the scan. The scanning laser is never able, therefore, to measure a perfectly vertical discontinuity.

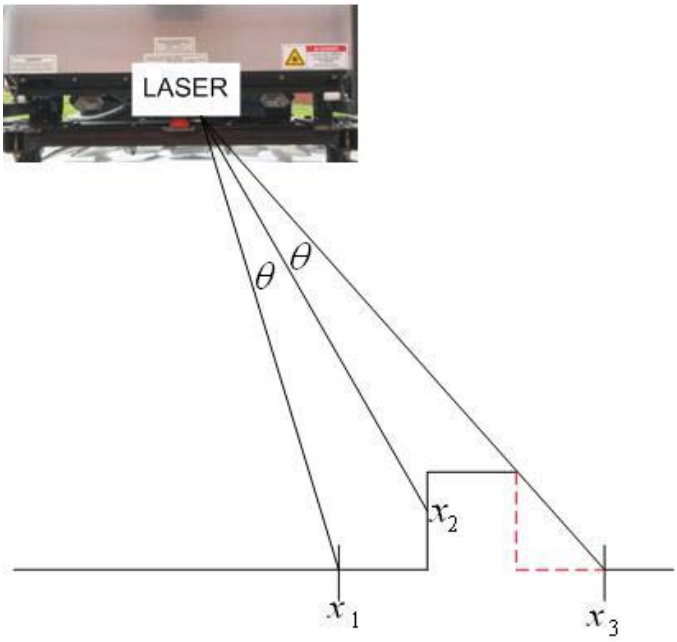

Figure 3-13: Transverse Slope Limitation Schematic

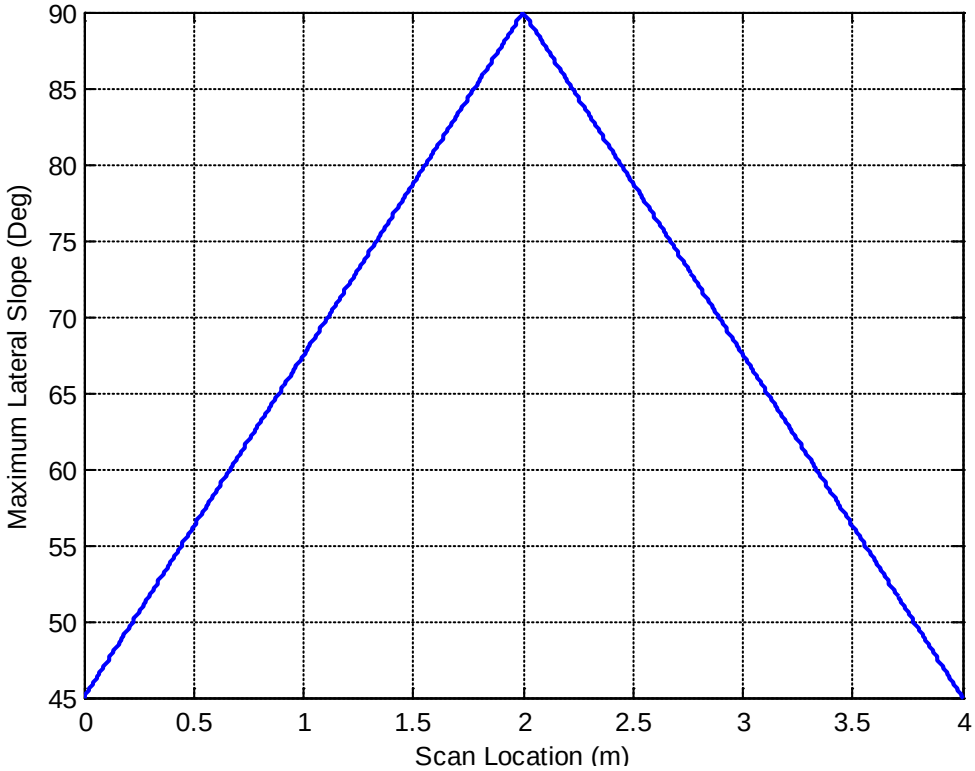

Figure 3-14: Lateral Slope Limitations for Scanning Laser

A calibration surface that meets the specifications is seen in Figure 3-15. The plate is specifically designed for the VTMS in Figure 2-1. The plate contains several sharp-edged events and the profile is known to sub-millimeter tolerance. It is recommended that the sharp transitions are about 15 millimeters in height. The surface is mostly black, except for the triangle and semi-circle which are light gray and more reflective. The mounting plate and two rectangular cleats in Figure 3-15 are all constructed of aluminum. The semi-circle and triangular cleats are both constructed from steel to be more cost effective. The plate contains counter sunk holes on a 152mm by 152mm grid to allow for cleat interchangeability while also maintaining ability to lie flat on the ground. Four steel handles are easily inserted and removed at each corner of the calibration surface to increase portability.

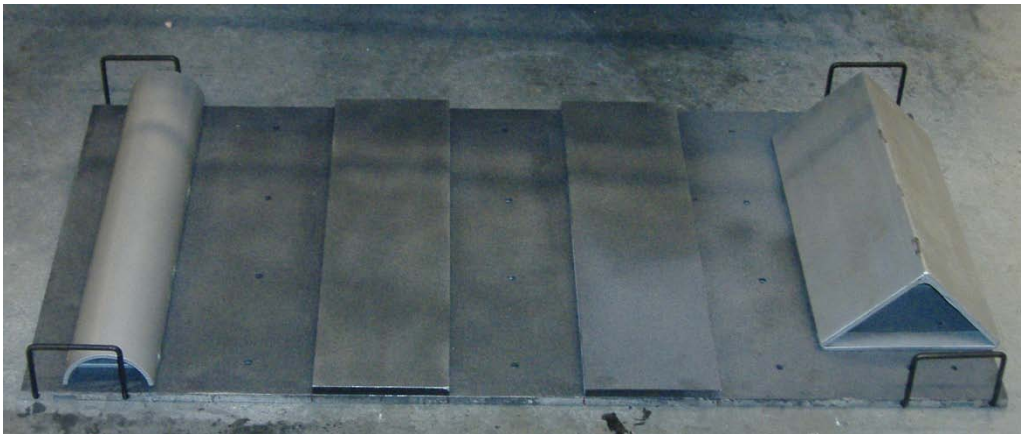

Figure 3-15: Sample Surface for Transverse and Longitudinal Calibration

3.5 Implementation Example

Using the excitation events and calibration surface developed above, a testing procedure is developed for the VTMS (shown in Figure 2-1). First, the laser's limitations are statically assessed in the transverse direction. This laser test is intended to fulfill requirements 1) and 2) of the calibration surface requirements developed in Section 3.4. The dynamic test consists of driving the vehicle over the excitation events (to induce high amplitude vibration) while simultaneously measuring the calibration surface. This test is done after the laser's capability is assessed so that the positioning system's limitations are independently verified.

In this chapter, the machined profile is compared to the profile as measured by the laser. The error between these signals is evaluated using the root-mean-square (RMS) of the error and maximum error.

3.5.1 Static Laser Verification Tests

In the laboratory, the calibration surface was placed transversely underneath the laser scanner on a level surface. The configuration for the static test is shown in Figure 3-16. The surface was placed approximately in the center of the laser scan.

Figure 3-16: Static Verification Test Configuration

First, the precision of the system is assessed. The plate is measured 4,000 times (approximately a 4 second test) and the standard deviation over the plate is calculated. Figure 3-17 is a plot of the mean profile (in blue) and the standard deviation (in green). The spikes in deviation occurred at the sharp transitions (as was expected) and on the more reflective surfaces (the triangle and semi-circle). The peak deviation is 1.2 mm.

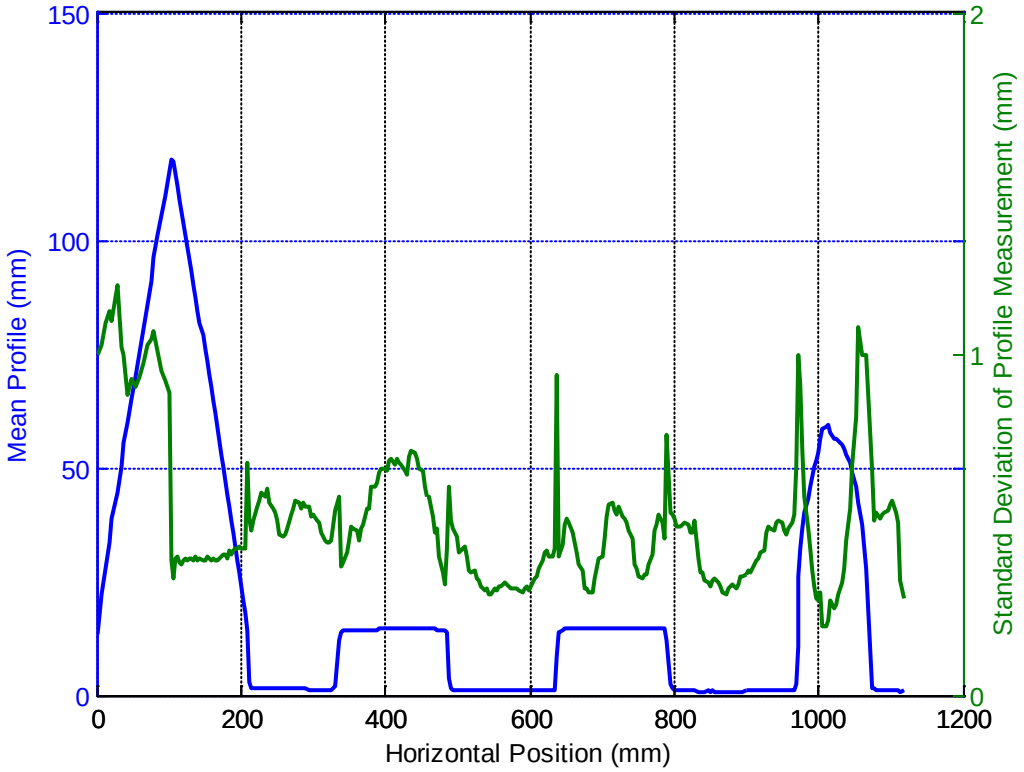

Figure 3-17: Comparing the Mean Profile and the Standard Deviation

The error signal and the machined profile are plotted in Figure 3-18. The error is very low except for large spikes on the inside of the semi-circular cleat and at the 90 degree transitions. The circular cleat is light in color and thus returns more energy to the receptor than if it were less reflective. Additionally, the location on the circle where high error is exhibited is normal to the laser's dispersal trajectory. This situation results in a saturated laser receptor and an inaccurate reading at that point. The peak error for this run is 5 mm and the RMS error is 1.1 mm.

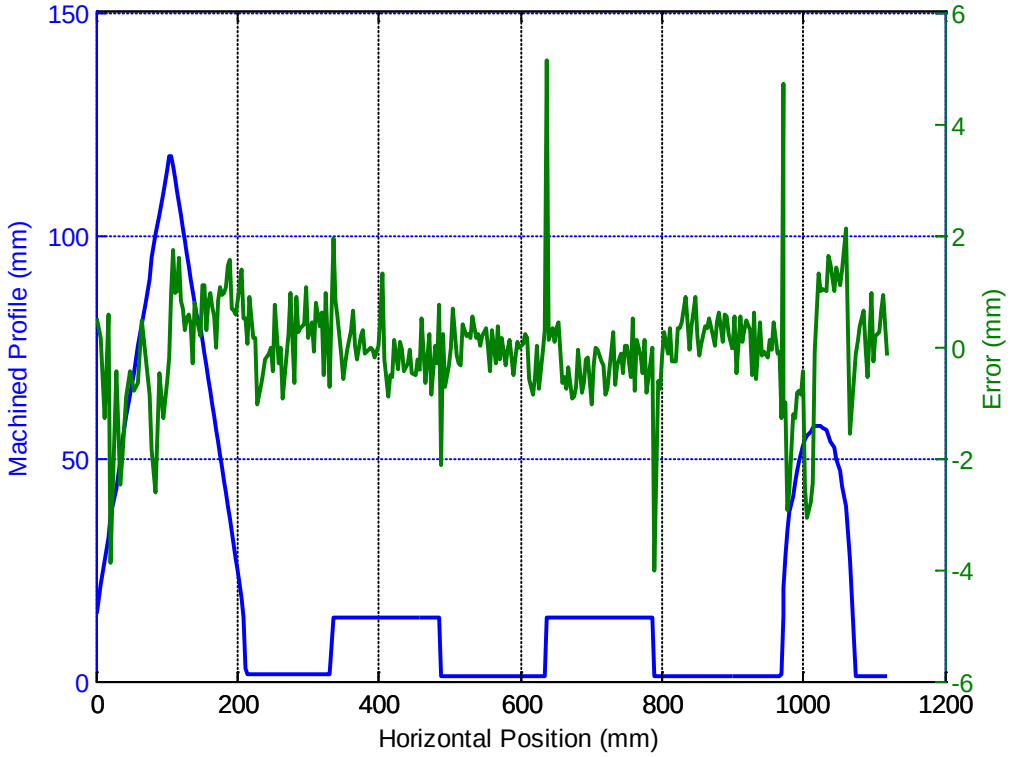

Figure 3-18: Comparing the Error Signal and the Machined Profile

While some of the error at the sharp transitions is due to the laser's inability to measure a vertical profile, the error can primarily be attributed to the way in which the machined surface is being compared to the measured surface. For each scan, the machined profile and the measured profile may not be perfectly aligned. This problem is due to the fact that horizontal precision of the laser is being coupled with the evaluation of the vertical accuracy.

Painting the reflective cleats the same color as the balance of the plate attenuates the error signal and thus improves evaluation metrics. Figure 3-19 performs the same transverse test as outlined above; however, the color of the plate is now homogeneous. The slight disagreement on the semi-circular and triangle cleat in Figure 3-18 is largely attenuated and the RMS error falls to 0.92 mm. The maximum error, however, does not change much due to the above mentioned alignment problem.

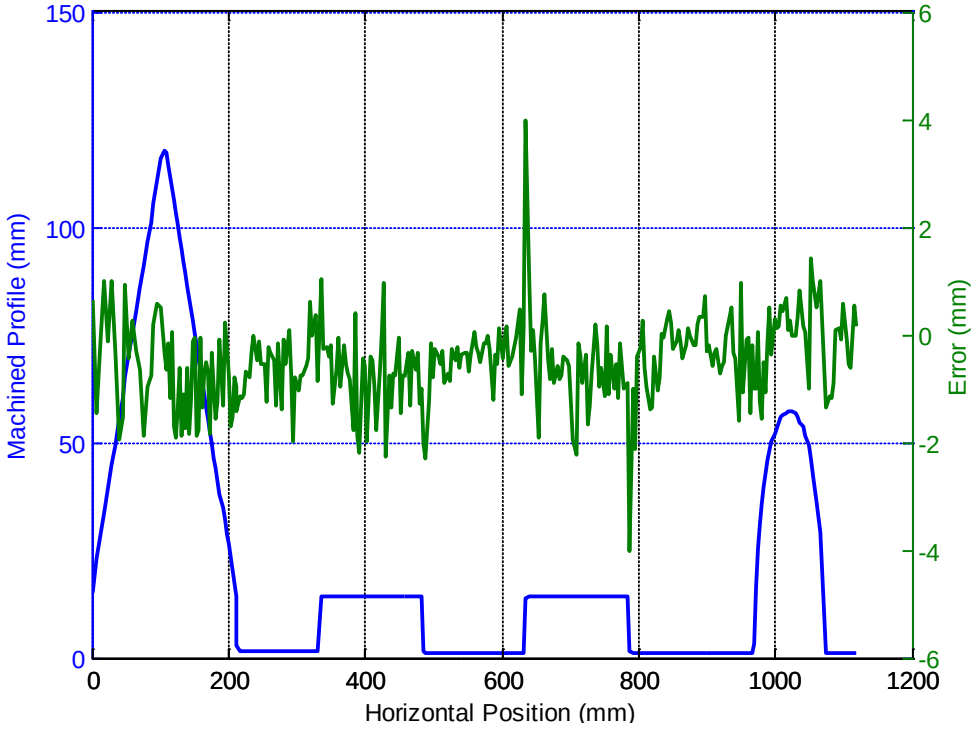

Figure 3-19: Profile Comparison- Homogeneous Color Scheme

3.5.2 Dynamic Verification System Test

Before the vehicle is subjected to the large amplitude vibration induced by the excitation events, the vehicle is driven longitudinally over the calibration surface to acquire measurements with no excitation. The spot size of the laser is 1.5 mm transversely by 10 mm longitudinally, thus lower accuracy is expected in the longitudinal dynamic testing (even if the common mode of the host vehicle motion is perfectly rejected). The RMS error of this test is 1.6 mm. This is the highest attainable accuracy of VTMS longitudinally (with its current configuration).

Figure 3-20 is a plot of the displacement of the laser as the vehicle traverses the excitation events. The excitation events induce nearly 200 mm of vertical displacement at the laser measurement system. This plot is shows the magnitude of the signal that must be rejected from the laser measurements.

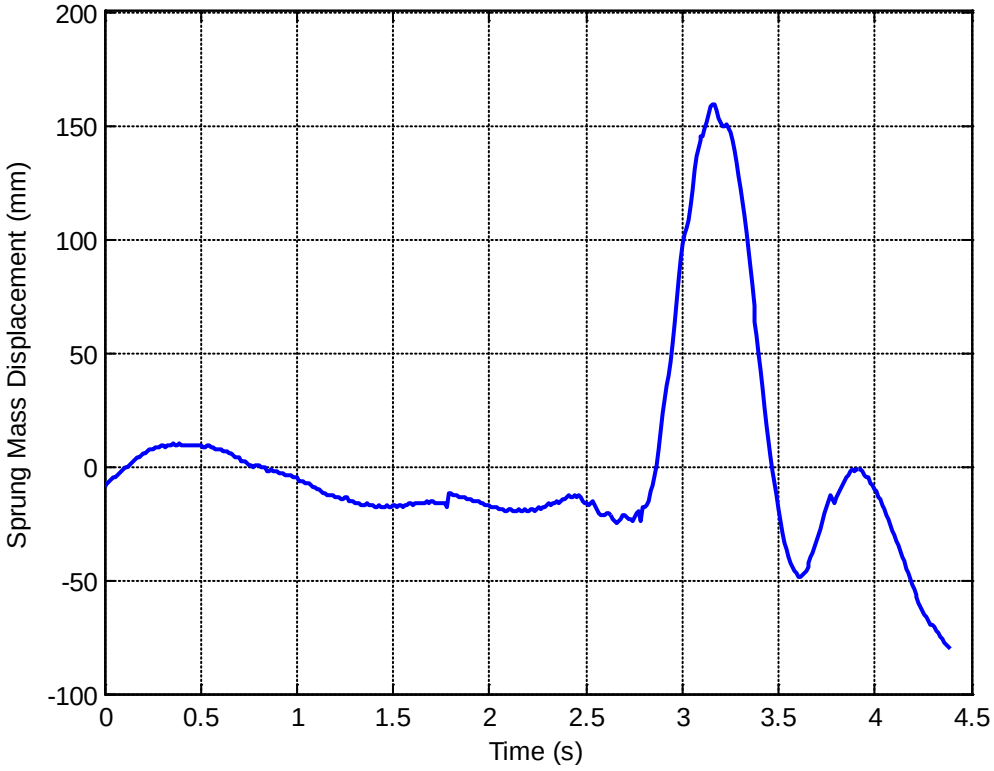

Figure 3-20: Sprung Mass Displacement over Excitation Events

For the dynamic verification test, the excitation events are placed in each of the vehicle's wheel path as it traversed the calibration surface. This configuration, as seen graphically in Figure 3-21, excites the vehicle near resonance while simultaneously requiring the system to acquire terrain measurements. When executing this test, the excitation events need to be secured to insure that the vehicle is not damaged.

Figure 3-21: Dynamic Verification Test

A 2D terrain profile is extracted from the 3D terrain surface for the purpose of profile correlation (2D profile extraction is developed in Chapter 5). The spacing of the 2D terrain profile at a host vehicle velocity of 13 MPH is set to 10 mm. While a higher point density could be obtained by driving the measurement system at a slower velocity, the vehicle would no longer hit its resonant frequencies as described in Equation (3-16). Figure 3-22 compares the measured profile to the machined profile for the dynamic test.

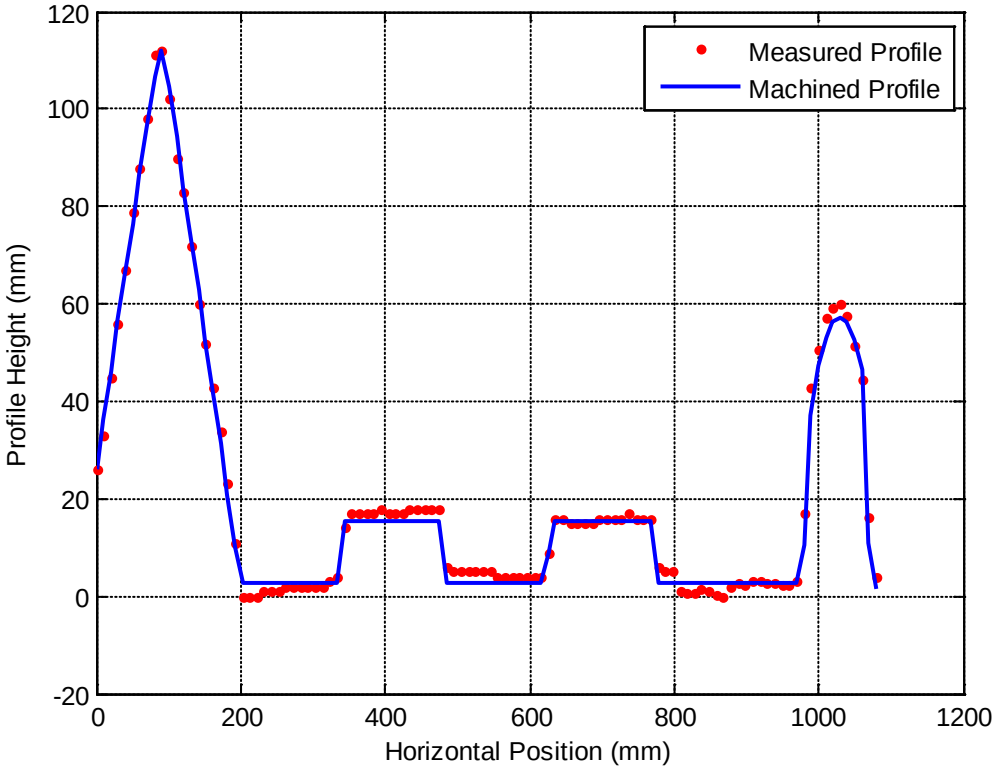

Figure 3-22: Comparing the Machined Profile to the Measured Profile- Dynamic Test

Figure 3-23 plots the error signal for the dynamic test. As expected, the highest error occurs at the steep discontinuities. The RMS error for this run is 1.95 mm and the maximum error is 5 mm. For the VTMS as is currently configured, the worst-case vertical accuracy in the longitudinal direction is less than 2 millimeters.

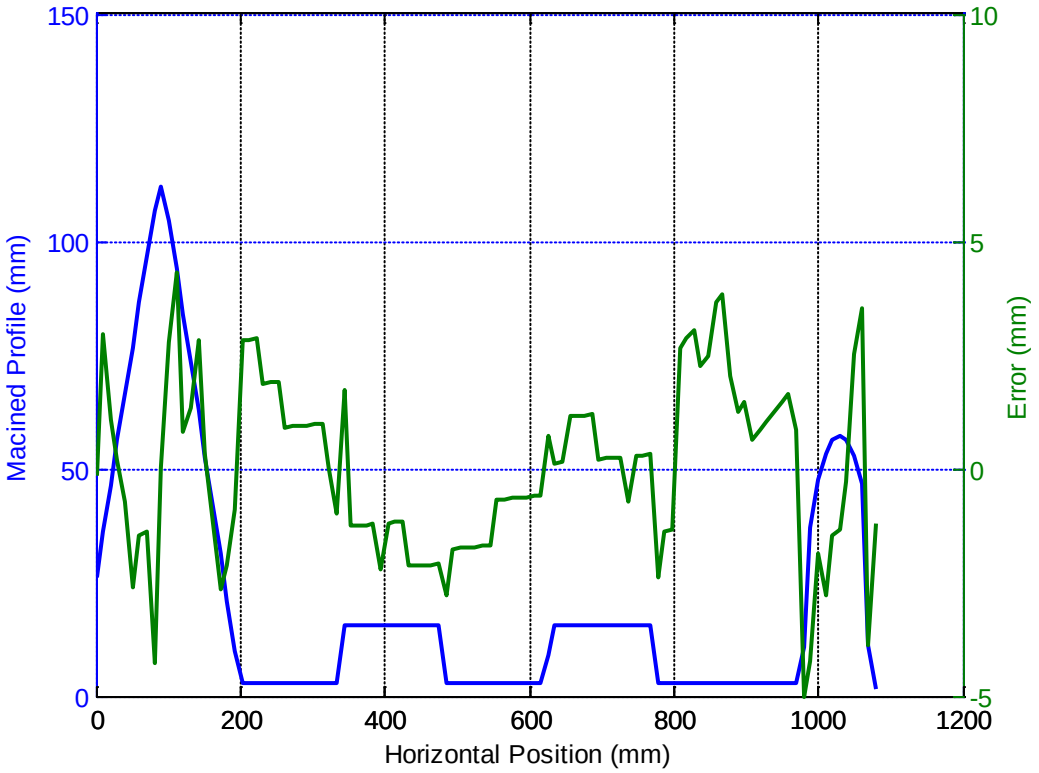

Figure 3-23: Error Signal- Dynamic Test

The accuracy test results for the VTMS are summarized in Table 3-1.

Table 3-1: Accuracy Test Summary

Test	RMS Error (mm)	Max Error (mm)
Static Heterogeneous Color	1.1	5
Static Homogeneous Color	0.92	4.3
Dynamic Uneventful	1.6	4
Dynamic Eventful	1.8	5

3.6 Chapter 3 Discussion

This work only considers validating terrain profilers for short runs (i.e., <<1 km). More research is needed to quantify terrain profiler performance over runs of a kilometer or longer. These long runs will inevitably suffer from equipment drift that will cause inertial errors in the data sets. The next chapter in this work develops methods to correct these inertial errors in the terrain data; however, no attempt is made in this work quantify system accuracy at long distances.

The excitation events were only configured such that the first two heave modes of the vehicle were excited. A more thorough test must be done which seeks to excite the vehicle's pitch and roll modes as well. The roll mode could be easily excited by staggering the existing events. Additionally, the excitation events must be traversed at a variety of longitudinal velocities to ensure that the profiler is validated at a range of frequencies.

The saturated condition that occurred over the reflective semi-circular cleat in Figure 3-18 could be addressed in post-processing. In addition to a profile output, the laser scanner also can output an intensity reading. If the intensity information is combined with the profile information, the profile points above or below some intensity threshold could be removed to improve the measured data set. This problem will be addressed in future work.

3.7 Chapter 3 Conclusions

This work provides the first step in assessing the accuracy of the data generated by modern inertial profilers. The excitation event assures that the vehicle is excited to its highest attainable amplitude (near resonance); thus requiring the body motion cancellation equipment to remove the maximum range of vehicular vibration. When used in conjunction with a calibration surface, the excitation event allows the user to describe the overall system accuracy, as well as the accuracy of each individual component.

If damping and frequency ratios are assumed, the mathematics behind the excitation event simplifies significantly; this assumption requires five uniformly spaced cleats. The cleat height is available as a selectable parameter; based on the developed design criteria, the height should be set at 19 or 38 millimeters so standard sized lumber can be used. Once the operator determines an overall excitation event length, the geometric properties of the event are completely constrained. This result means that the event is easily constructed from quickly attainable and inexpensive materials.

The highest error increase came at the introduction of the dynamic test. Several parameters changed from the static test to the first dynamic test. First, the orientation of the calibration surface was changed. Second, and more importantly, the dynamics of the

vehicle were introduced to the laser measurements. While the spot size of the laser probably accounts for some of the error increase, the majority of the error can be accredited to the positioning system. This conclusion is supported by the fact that the most signal power can be seen at the vehicle's wheel-hop frequency. More research is needed to modify the system to better mitigate body motion.

4. Correcting and Averting Inertial Errors

4.1 Chapter 4 Introduction

The primary objective of this chapter is to develop a method for reducing lane misalignment due to INS drift. The remainder of this chapter is developed as follows. First, a brief overview is presented on the evolution and practical applications of 3D terrain surfaces and eliminating the host vehicle's body motion from the laser measurements. Next, the method for combining multiple lanes of data is developed. Additionally, techniques are presented for effectively handling the large file sizes generated by 3D terrain measurement systems. Pavement health monitoring is discussed in the context of INS inaccuracies, followed by concluding remarks.

4.2 Chapter 4 Background

For terrain measurement systems, an INS solution is used to estimate the laser's position and orientation in a device-centered coordinate system. The INS is capable of accurately determining geodetic position to within 2 cm. Traditional inertial measurement systems rely only on accelerometer data to remove unwanted body motion from post-processed data files. The reliability of a system solely using accelerometers to remove body motion suffers when vehicle speed falls below 5 m/s [41] and in other low frequency environments. To remedy this poor reliability, the VTMS exclusively uses the INS data to mitigate low frequency motion, and three coplanar accelerometers augment the INS solution for mitigating high frequency motion. This arrangement bolsters the INS solution with additional high frequency information and does not suffer from the low frequency issues common to traditional accelerometer-based systems.

The laser measures the relative distance between itself and the terrain surface (both vertical and transverse distance) in device-centered coordinates; it does not collect data concerning its absolute location in space. The accelerometers and the INS also have

their own associated device-centered coordinate system. To establish a common coordinate system, the origin of the device-centered coordinate system corresponding to the accelerometers and to the INS must be translated to the laser. Once the data from each device are translated to the laser and synchronized in time, the host-vehicle body motion information is removed from the laser data. Finally, a coordinate transformation assigns each measured data point a location relative to the base station antenna of the INS. The global coordinates are defined such that the horizontal and vertical coordinates have their positive sense in the Easting and Northing directions, respectively. Figure 4-1 demonstrates the end data result of the VTMS. In this figure, the large rectangle is digital photograph, and the superimposed, tilted, small square is a rendering of the corresponding measured data. The rendering is generated by loading a measured terrain surface into a commercial visualization software package. In the figure, the measurement detail is seen from the cracks between the blocks to the roughness of each block.

Figure 4-1: Terrain Image and Overlaid Terrain Rendering

4.3 Correcting for Instrumentation Misalignment and Inertial Drift

Small errors in the INS data skew the absolute location of the terrain surfaces in the global reference frame. For independent lane scans, this problem may not affect the application of the terrain data, since absolute location may not be of interest (e.g., for

vehicle ride and durability studies). If a measurement, for instance, is taken over perfectly level terrain for one kilometer, a slowly varying height change of several millimeters does not hinder simulation effectiveness. However, if data are recorded along the first lane of a two lane highway early in the day and the second lane is measured late in the day, then any vertical misalignment of the two lanes resulting from the slowly varying height change produces an artificial vertical shift between lanes. While this vertical misalignment may not greatly affect simulations in which the vehicle remains in the same lane, the misalignment between the two lanes would cause undesired excitations into a model undergoing a lane change maneuver.

4.3.1 General Correction Technique

When two adjacent lanes of data are desired, the data must be acquired so that there is an overlapping section of terrain. Inertial drift may cause disparities in the measured heights in this overlapping section. That is, at each horizontal location in the overlapping section, the height acquired during the measurement of lane 1 is different than the height acquired during the measurement of lane 2. This problem is illustrated via the Belgian block terrain shown as a rendering in Figure 4-2. When the surface is examined in plan view, two discontinuities, corresponding to the boundaries of the overlapping region, are seen in Figure 4-2.

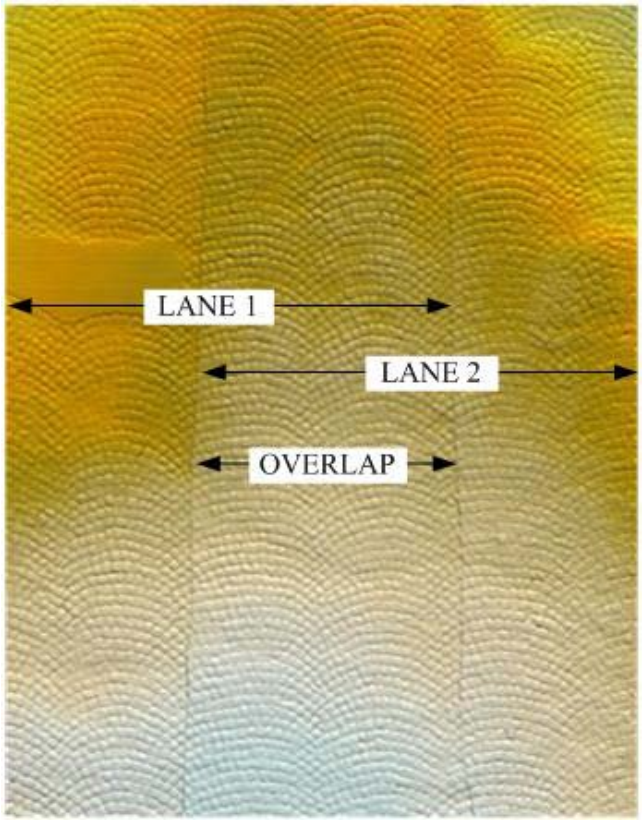

Figure 4-2: Two Lanes of Misaligned Belgian Block Data

The first step in this method is to prescribe a reference path and reference path points through the overlapping section of terrain. A small section of overlapping terrain is shown Figure 4-3 to demonstrate the prescription of the reference path as a simple linear function; however, it can be prescribed in a variety of ways. For example, a sequence of discrete waypoints can be established along the center of the overlapping section. In this case, a continuous path function must be established using a piecewise cubic Hermite interpolating polynomial (PCHIP) or some other interpolator. Next, specific points along the reference path are defined. The spacing of these reference path points must be defined such that the point density is high enough to fully characterize the lane-to-lane discontinuity. However, if the point density is excessive, the correction procedure will be computationally inefficient. Regardless of the manner in which the reference path is prescribed, the reference path points are chosen so that they are equally spaced in the horizontal plane to improve computational efficiency in implementing the

next step in the method. For more developmental information on prescribing a path, see Chapter 5.

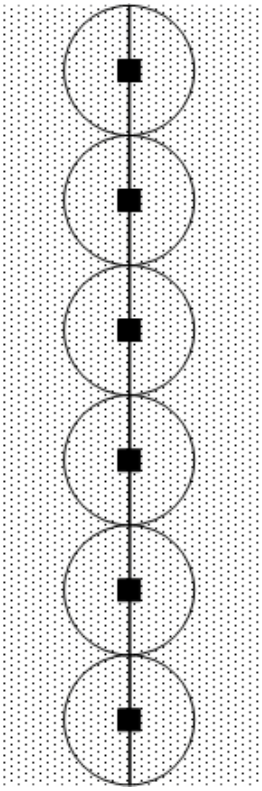

Figure 4-3: Defining a Reference Path and Search Area

At each reference path point, local height measurements are used to estimate the reference height. A search area in the horizontal plane (shown as a circular region in Figure 4-3) is constructed to sample the height values in the region surrounding each reference path point (shown as a solid black square in Figure 4-3). The reference path and search area must be chosen so that no points in the search area lie outside of the overlapping region. Samples of local height measurements form a distribution of estimates of the reference height for each reference path point. This distribution is represented as a frequency histogram in Figure 4-4 where the height values in the search area from the lower lane (this set is designated $\boldsymbol{z}^{(1)}$) are blue bars and the red bars represent the heights in the search area from the higher lane (this set is designated $\boldsymbol{z}^{(2)}$).

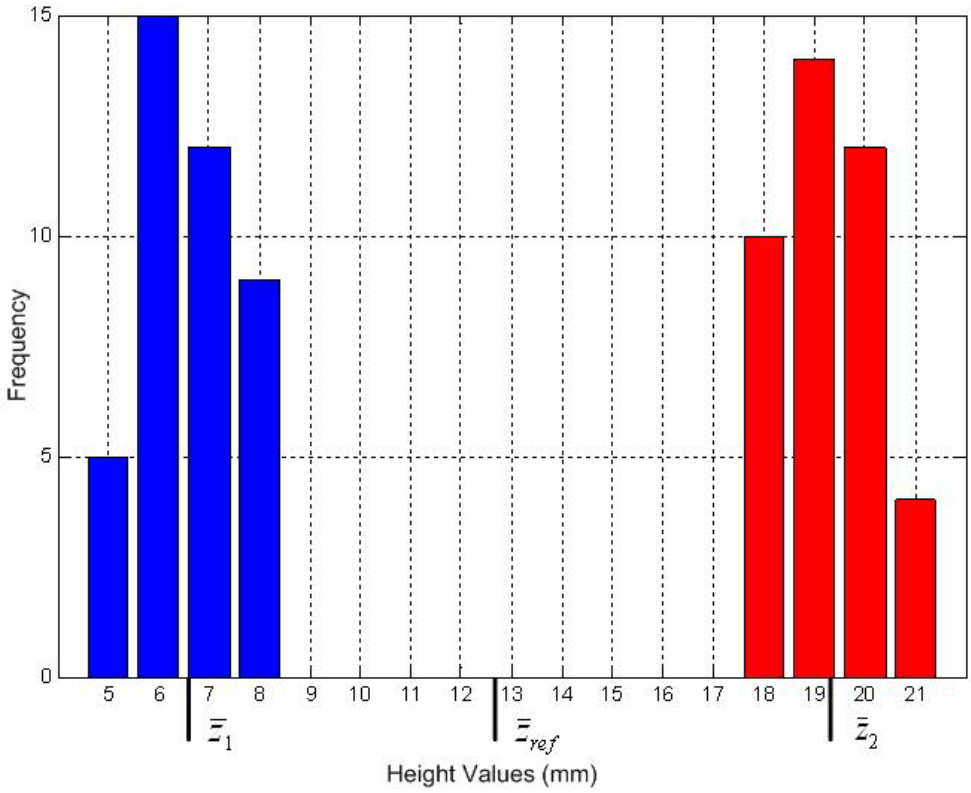

Figure 4-4: Histogram of the First Reference Path Point

Several methods can be used to define the reference height based on this distribution. In this work, the mean value, $\bar{z}_{ref}$, in Figure 4-4, is selected as the best estimate of the reference height. In Equation (4-1), a reference height is calculated using the height values from each lane.

$$\bar{z}_{ref} = \frac{1}{n_1}\sum_{i=1}^{n_1} z_i^{(1)} + \frac{1}{n_2}\sum_{j=1}^{n_2} z_j^{(2)} \tag{4-1}$$

Now consider a lane of data (e.g., lane 1 in Figure 4-2) that has several height measurements lying within the search area of a particular reference point. It is desirable to change the height of the lane in the neighborhood of this reference point to align with the reference height. Several heights are estimated at this reference point during the measurement of this lane, but one height must represent the height of this lane at this reference point. The mean height from the measurement of this lane is selected to represent the height of the lane at this reference point. In this example, the mean heights

for each lane are displayed as $\bar{z}_1$ and $\bar{z}_2$ in Figure 4-4. The average height differences for each lane at this reference point are then $\left(\bar{z}_1 - \bar{z}_{ref}\right)$and $\left(\bar{z}_2 - \bar{z}_{ref}\right)$ and these differences are calculated for each lane at each reference point.

The average height difference values for each reference path point are compiled into a discontinuity vector for each lane that defines how the heights in each lane of data should be adjusted along the reference path. A generic discontinuity vector is shown as a solid line in Figure 4-5. In practice, the discontinuity vector contains high frequency noise and requires low-pass filtering. After filtering, the discontinuity vector provides information for adjusting each point in the lane (as shown as a dotted line in Figure 4-5). This correction procedure is applied to every point in the lane to achieve proper alignment.

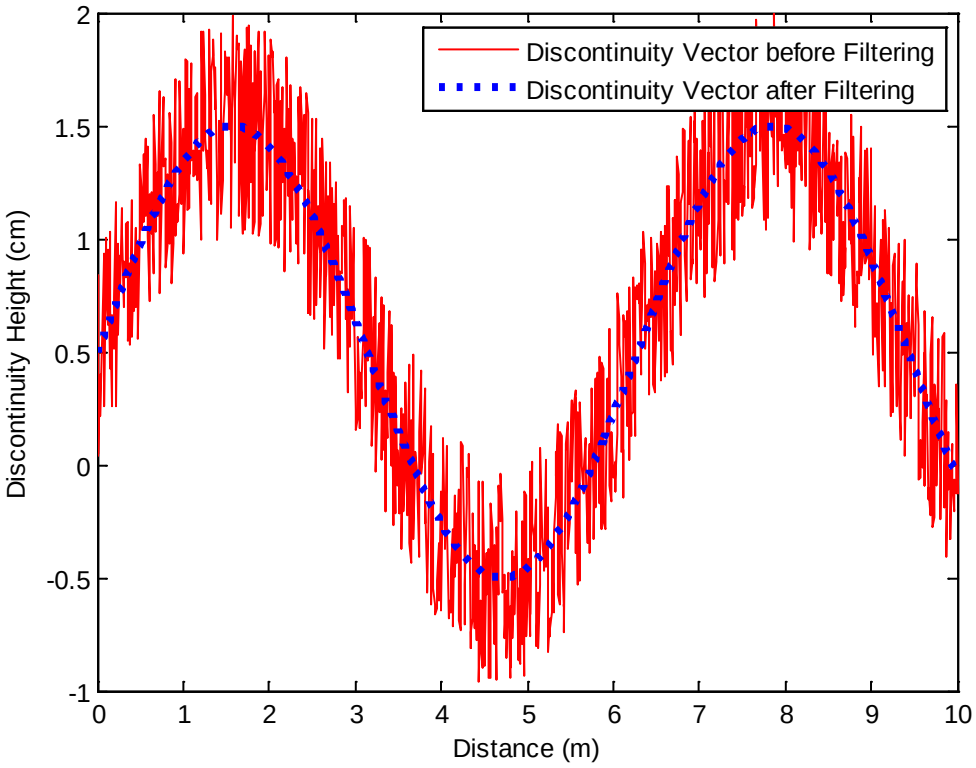

Figure 4-5: Generic Discontinuity Vector

Implementing the above developed procedure on the two lanes of data in Figure 4-2 generates the surface in Figure 4-6. The discontinuities that formerly existed at the boundaries of the overlapping region are reduced to 1 millimeter or less. The two distinct

lanes have been successfully merged into one continuous surface. This method effectively corrects inertial artifacts in any terrain type.

Figure 4-6: Two Corrected Lanes of Eventful Terrain

4.3.2 Correcting Smooth Terrain

The method developed in Section 4.3.1 effectively eliminates discontinuities for any terrain type; however, if the application requires a lower resolution (e.g., a racetrack where only bank and pitch angles are only sought), then a more computationally efficient method can be employed. Figure 4-7 is a visualization of two concatenated lanes of high-resolution highway data. In general, the highway data are smooth and do not contain small localized disturbances. Again, the overlapping region is designated by the two discontinuities in Figure 4-7.

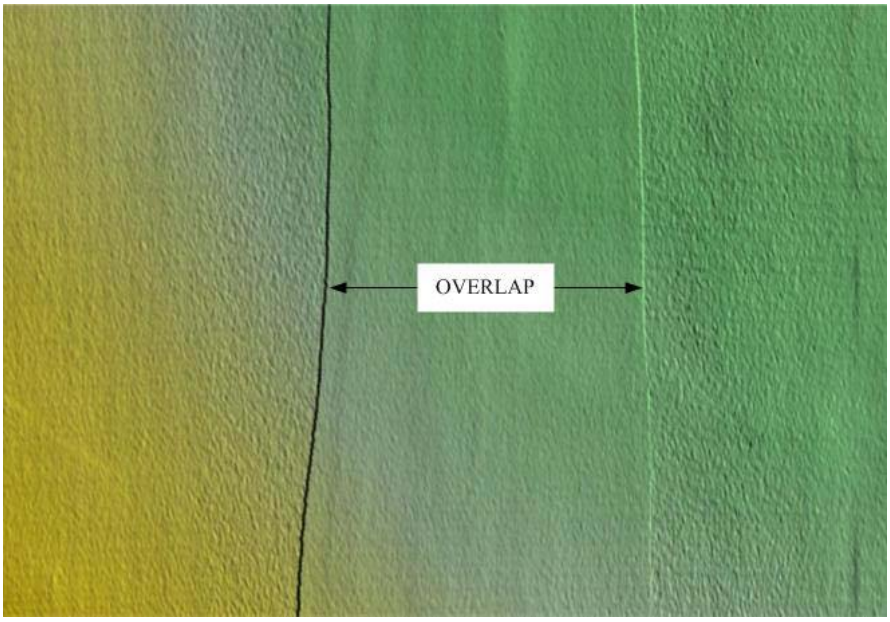

Figure 4-7: Adjacent Lanes with Vertical Discontinuity

Current systems measure terrain with a horizontal resolution of 5 mm, effectively capturing localized disturbances; however, when the terrain topology does not contain these disturbances, the measured terrain can be down-sampled with negligible loss of information. The method developed in this section proposes to eliminate INS artifacts by using a mean interpolation technique to take the high-resolution data to a lower resolution.

The measured terrain must be sufficiently sampled so that the desired resolution of the final data set is coarser than the sampled data before a mean interpolation technique is applied. Next, the horizontal locations of the final data set are fixed, preferably on a uniform grid [42]. This gridding method allows the data to be stored much more efficiently and thus is advocated in this work. For each grid point, samples of local vertical measurements are used to estimate the final vertical location of that grid point. In this chapter, a search area in the horizontal plane is constructed to define the vertical measurements that are considered for this estimate of the final vertical location. Once these vertical measurements are identified, they constitute a sample of the true vertical values that exist at that horizontal location. A statistic must be chosen to best estimate the height of the point. In this work, the arithmetic mean is selected to represent this height. By selecting the mean, any small lane-to-lane discontinuity is removed in the

gridding process. This concept is illustrated in Figure 4-8 where the small points represent measured data, the squares represent the desired uniform grid nodes at which a height must be computed, and the circles represent the search area for each grid node. Figure 4-8 is point representation of the terrain surface in Figure 4-7. Each uniform grid node is determined by finding the mean of multiple sampled data points.

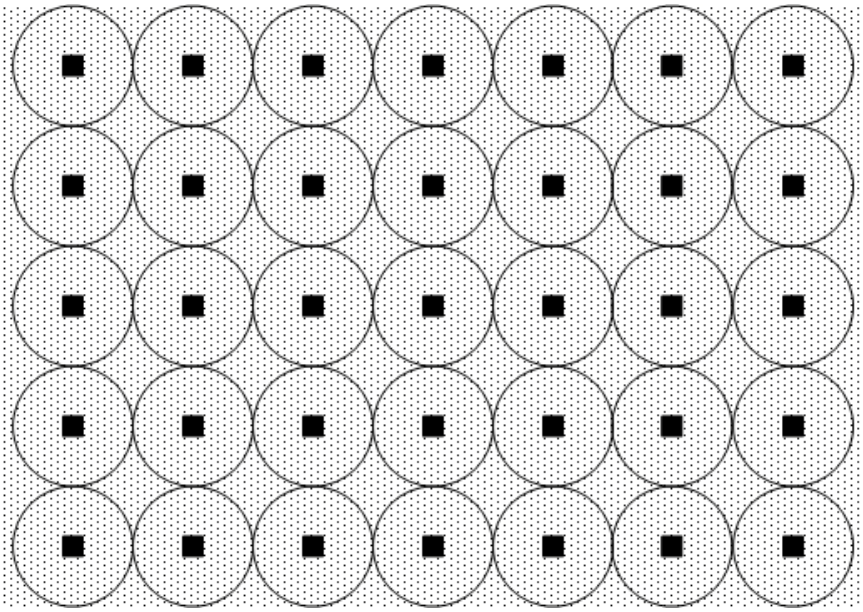

Figure 4-8: Implementing the Mean Interpolation Method

Figure 4-9 is generated by performing this mean interpolation technique on the data in Figure 4-7. The discontinuities that existed in the original data set have been eliminated; after correction, the transition between lanes in the concatenated set is smooth. Note that in removing the artifacts from the INS drift, the resolution of the data set has decreased.

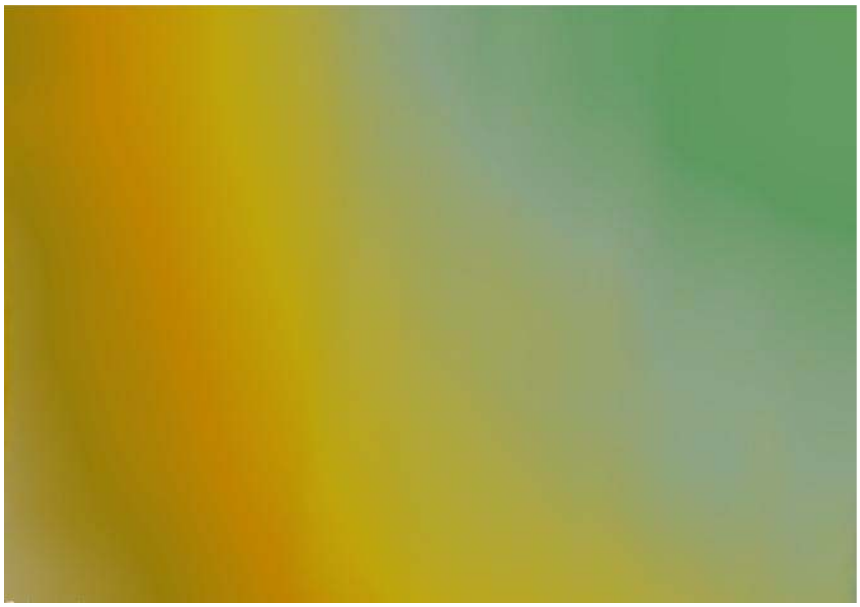

Figure 4-9: Discontinuity Removal via a Mean Interpolation Method

4.4 Chapter 4 Discussion

When correcting eventful terrain, carefully prescribing a reference path will greatly simplify the correction process. For instance, if data acquisition begins and ends at the same point (e.g., an oval racetrack) then a reference path is prescribed easily if the data are transformed to polar coordinates. This coordinate frame allows the user to collect lane discontinuities using angular intervals instead of longitudinal distances between path points. This concept can be expanded to concatenate three or more lanes of data. In this case, separate discontinuity vectors are built for each pair of adjacent lanes.

It is desirable to minimize the systematic errors that lead to inertial errors and critical, therefore, that each piece of equipment be carefully installed and calibrated during development of a terrain measurement system [16]. Test runs should be recorded which seek to physically align the instrumentation using the results of the post-processing phase [7]. It should be clear that perfect alignment of subsystems is impossible and therefore, cumulative errors in the data sets must be addressed.

In addition to providing accurate vehicle simulation excitations, terrain measurements are effectively used as a means to monitor pavement health. Currently, road profilers with single-point lasers are used to measure road roughness. These lasers capture localized disturbances of all sizes, including those that are mechanically filtered

in the physical vehicle system. The longitudinal profile that results from optically measuring this disturbance does not accurately describe the way in which the terrain excites the vehicle. Algorithms have been proposed to consider the effects of tire bridging and envelopment [2, 23, 43]; however, these statistical methods may attenuate actual profile roughness and do not consider all of the information in a vehicle's wheel path.

Large file sizes are also a factor to be considered when working with 3D terrain surfaces. For a smooth surface that is going to be characterized by bank angles and terrain pitch (e.g., an asphalt racetrack), the data can be systematically reduced by down sampling the data set. Down sampling can also be accomplished by relaxing the grid spacing requirements. Down sampling by an order of magnitude or more may not alias any frequency content of a surface characterized only by bank angles and terrain pitch.

4.5 Chapter 4 Conclusions

The techniques developed in this work address the needs of emerging 3D terrain measurement applications. For precise terrain measurement, even the most accurate equipment introduces errors that adversely affect simulation data. These errors must be identified and removed to assure that the simulated vehicle experiences the same excitations as a real vehicle. This chapter develops a general technique to correct misalignment between adjacent lanes of any terrain type. Additionally, a more computationally efficient method is developed for adjacent lanes of smooth terrain. While much more computationally efficient, care must be used when implementing the smooth terrain method because localized disturbances in the terrain are attenuated. One major benefit of the techniques developed in this work is a reduction in the data required to represent the measured terrain topology.

The ability to combine multiple lanes of terrain data provide the automotive engineer with the capability to simulate a vehicle in a variety of environments ranging from proving grounds to multi-lane highways. Since the terrain surface is the primary source of excitation for the vehicle system, high-fidelity terrain measurements are critical for accurate simulations. Improving simulation quality leads to better information

throughout the design process and ultimately enhanced vehicle designs at a fraction of the cost.

5. Mapping a 2D Profile from a 3D Terrain Surface by Emulating a Tire's Mechanical Filtering Properties

5.1 Chapter 5 Introduction

Clearly, 3D terrain measurement systems outperform 2D terrain profilers when characterizing a terrain surface; however, these 3D systems produce copious amounts of data [42, 44] that lead to computationally intensive simulations. This problem is exacerbated by the fact that few 3D terrain measurement systems currently exist, so performance metrics are not well defined. While complex multi-body dynamics and tire models require high-fidelity 3D terrain surfaces, the data are impractical for simpler ride and handling simulations.

Conversely, 2D terrain profiles are relatively simple to acquire and process and cross-correlation performance metrics have been rigorously evaluated [2-4]. Additionally, 2D terrain profiles provide vehicle dynamicists with fast computationally efficient model excitations. Unfortunately, the point lasers used in these 2D terrain profilers are incapable of differentiating between small areas of localized disturbances (e.g., a small stone or crack) and larger disturbances that excite larger amplitude chassis vibration. Consider the tire envelopment example in Figure 5-1. The small stone seen in the upper photo is mechanically filtered by the tire and thus does not significantly excite the vehicle system; however, the corresponding 2D terrain profile shown in the lower plot exhibits a sharp spike that would deceptively lower any applied performance metric (such as the international roughness index or ride number) that does not account for the physical shape of the tire.

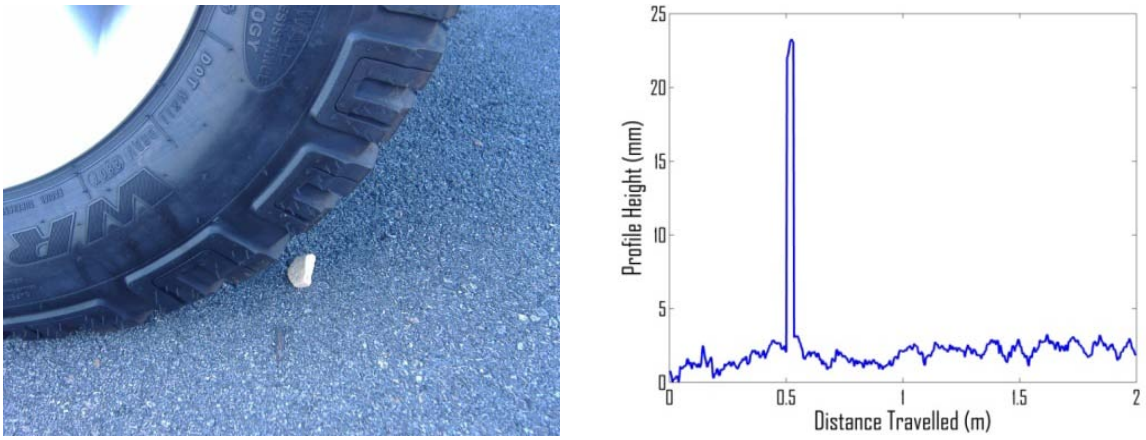

Figure 5-1: Tire Envelopment Problem

If the discontinuous profile is implemented in a simulation that used only a simple point tire model, the simulated vehicle experiences loads very different from the loads seen by the actual vehicle. Moving averages and other filters [2] have been proposed which filter the 2D profile in a way that emulates tire properties; however, these techniques fail to consider all of the information available in a tire's contact patch. Additionally, these filters fail to consider all of the information contained in the vehicle's wheel path.

The primary objective of this work is to develop a method for mapping 3D terrain surfaces to 2D terrain profiles that emulates the manner in which a tire samples the surface, such that undesired contributions from localized disturbances are attenuated. The remainder of this chapter proceeds as follows. The first step in mapping 3D terrain surfaces to 2D terrain profiles requires a path to be prescribed through the 3D terrain surface. Next, equally spaced points in the horizontal plane are created along the prescribed path. At each point in the prescribed path, heights are accumulated within a defined search area. The median value of these accumulated points is selected from the distribution of points to eliminate the effects of outliers that correspond to small localized disturbances. Finally, future work is discussed in which a deformable tire filter to better emulate the method by which tires experience the terrain.

5.2 Mapping 3D Terrain Surfaces to 2D Profiles

5.2.1 Prescribing a Path

The first step in this method is to prescribe a path through the 3D terrain surface. Consider a 15 meter long stretch of the 3D Belgian Block terrain surface depicted with the defined coordinate system in Figure 5-2. The longitudinal direction is defined as *y*, the transverse direction is defined as *x*, and the heights at each horizontal location are defined as *z*. A small section of this 15 meter stretch of terrain is selected for further consideration and is shown as the dashed parallelogram in Figure 5-2. This section is expanded and viewed in the horizontal plane in Figure 5-3.

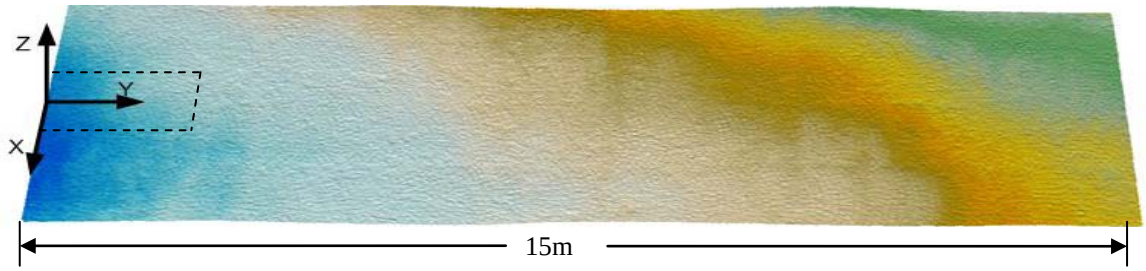

Figure 5-2: 3D Terrain Surface with Coordinate System Defined

The details of the path prescription are shown in Figure 5-3. The small dots represent the measured data points, the larger dots represent the path points along the solid black line that represents the prescribed path, and the search area for each path point is shown as large black circles encompassing each path point. The path in the horizontal plane can be prescribed in a variety of ways. For example, waypoints can be established through the data or a simple function can be used. If the user prescribes discrete waypoints, a continuous path function can be established using a piecewise cubic Hermite interpolating polynomial (PCHIP) or some other interpolator. Next, discrete points that are equally-spaced in the horizontal plane are defined along the continuous path function.

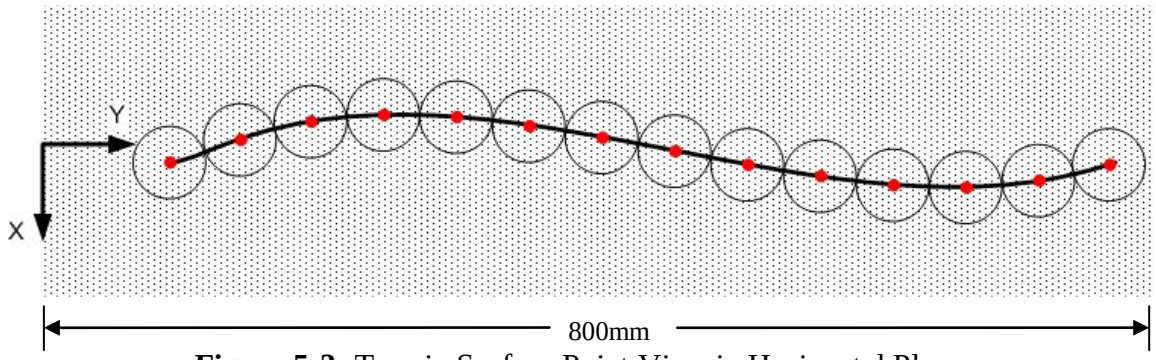

Figure 5-3: Terrain Surface Point View in Horizontal Plane

The result of this step is a path, *u*, defined on the 2D horizontal plane such that the locus of points that lie along the path are defined by *u(x,y)*. Individual path points are separated by a prescribed horizontal spacing *du*. The decomposition of *du* into its orthogonal components in the horizontal plane is *dx* and *dy*, as shown in Figure 5-4. The intersection of the *du* segment and the *dx* segment corresponds to one path point, and the intersection of the *du* segment and the *dy* segment corresponds to the adjacent path point.

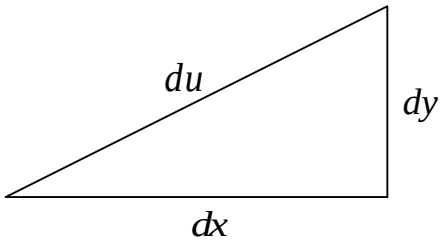

Figure 5-4: Determining X-Y Locations of the Reference Path Points

The spacing in the horizontal plane, dx_i and dy_i, is determined from the prescribed spacing, *du*, and estimating the local derivative of y_i with respect to x_i of the continuous path, $(dy/dx)_i$. This slope is estimated using the coefficients of the continuous path function. For instance, if the defined path is simply a line then *du* will be constant for every dx_i and dy_i. The relationship between dx_i, dy_i, and *du* is written explicitly in Equation (5-1).

$$dx_i^2 + dy_i^2 = du^2 \tag{5-1}$$

Solving for dx_i produces Equations (5-2) and (5-3).

$$du^2 \Big/ dx_i^2 = 1 + \left(dy \Big/ dx \right)_i^2 \tag{5-2}$$

$$dx_i = \frac{du}{\sqrt{1 + \left(dy \Big/ dx \right)_i^2}} \tag{5-3}$$

Similarly, solving for dy_i produces Equations (5-4) and (5-5).

$$du^2 = \frac{du^2}{1 + \left(dy \Big/ dx \right)_i^2} + dy_i^2 \tag{5-4}$$

$$dy_i = du \sqrt{1 - \frac{1}{1 + \left(dy \Big/ dx \right)_i^2}} \tag{5-5}$$

This procedure is repeated for each location along the prescribed path, thereby defining the location of the i^{th} path point as $u_i(x_i,y_i)$.

5.2.2 Determining a Height for each Path Point

For each path point, $u_i(x_i,y_i)$, height value, $z_i(u_i)$, must be determined. The desired search area is prescribed; then a distance vector, d_{ij}, from the path point $u_i(x_i,y_i)$ to each measured data point is found to ascertain which measured data points lie within the search area. $\hat{x}_j$ and $\hat{y}_j$ designate the horizontal locations of the measured data points. Equation (5-6) computes the distance from a reference path point, i, to each measured data point.

$$d_{ij} = \sqrt{\left(x_i - \hat{x}_j \right)^2 + \left(y_i - \hat{y}_j \right)^2} \tag{5-6}$$

A weighting function can be defined within the search area that emphasizes the influence of points that lie closer to the path point (e.g., inverse distance to a power); however, in this work, all points are assumed to be weighted equally. The size of the

disturbance that is bridged or enveloped by applying this method is adapted by changing the prescribed search area. For example, the stone in Figure 5-1 is about 25 millimeters in diameter. While some experimentation is required to select an appropriate search area, it is bounded by the size of the tire's contact patch. To properly parameterize the method such that the contributions are mitigated, the search area must have a diameter greater than 25 millimeters; this results in a search area greater than 500 mm^2.

The accumulated heights at each path point are ordered and the corresponding cumulative probability function (CPF) is developed [45]. The heights accumulated in the search area around the first path point in Figure 5-3 are represented graphically in Figure 5-5. Next, a value for the height of the terrain at this location must be selected such that it emulates the mechanical sampling of the tire. The CPF is used to identify that height. In this example, 81 points were found within a search area of 2000 mm^2 (corresponding to a radius of 25 mm). Note that the reference path points in Figure 5-3 are spaced coarsely for ease of viewing. The range of height values in this search area is 7 mm. If a small disturbance were measured, this variation would be much higher. In this work, the median value is proposed to represent the height at this path point. By selecting a statistic that is insensitive to outliers in the data, the effects of small localized disturbances is mitigated.

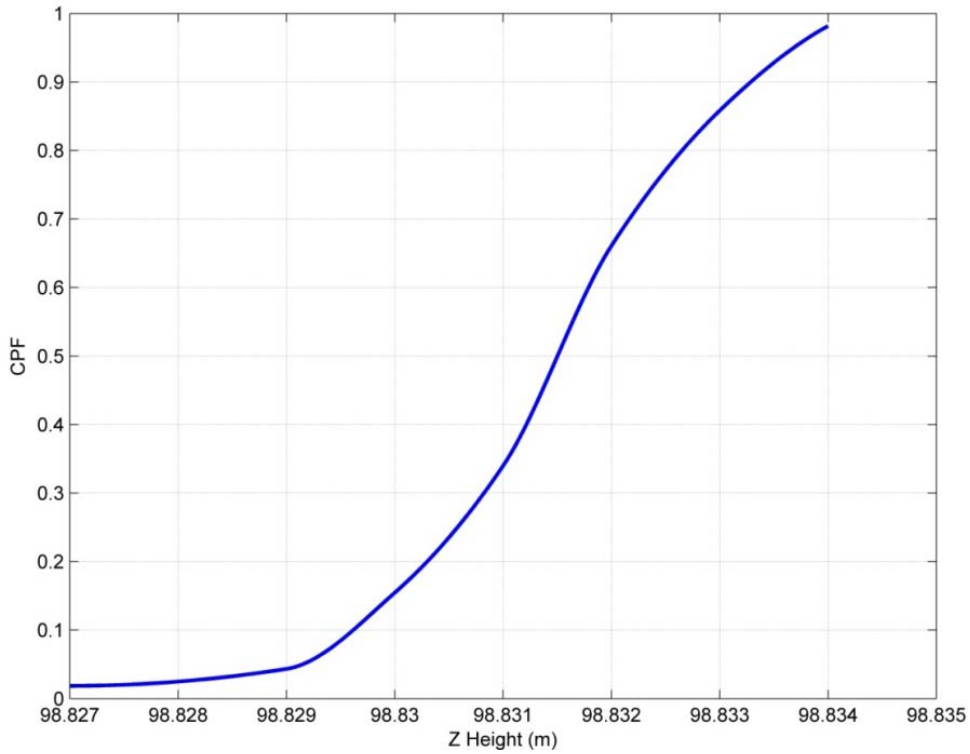

Figure 5-5: CPF for the First Path Point

The tire in the left photograph in Figure 5-6 is a schematic with color coded lines that correspond to different profile locations within the tire's contact patch. The right image in Figure 5-6 is a plot that contains each of these profiles over a section of Belgian block terrain (these profiles were not mapped using the method developed in this chapter). Any of these profiles potentially could be implemented into a vehicle simulation using a point tire model. In some locations, there is up to a centimeter of variation between the profiles. This variation arises from the laser measuring the block joints on the Belgian block surface. Figure 5-6 also demonstrates the 2D profile mapped from the 3D terrain surface (the yellow line). The mapped profile considers the information contained in the other profiles (in addition to the other profiles not plotted on this figure). Close examination of the mapped profile reveals that the sharp dropouts corresponding to the block joints have been attenuated.

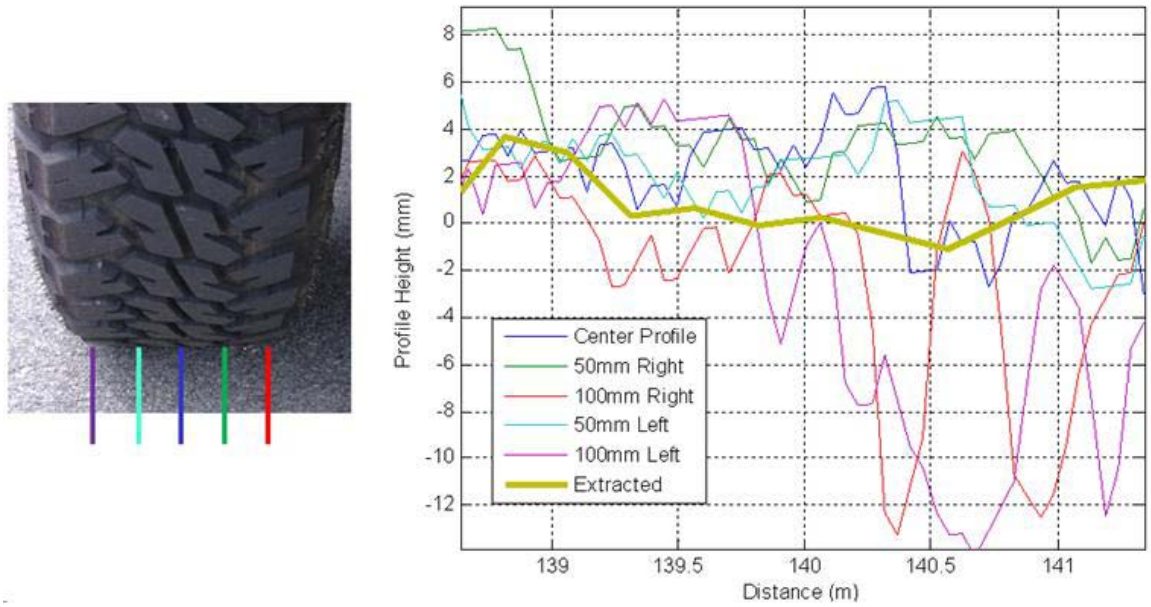

Figure 5-6: 2D Terrain Profile of Belgian Block

5.3 Chapter 5 Discussion

If the vertical resolution of the 3D terrain surface data is large when compared to the range of the vertical heights within the search area, then repeated height values will occur within the search area for each path point. The real terrain surface contains sampled heights along a continuum. In the example used in this work, the vertical resolution is set to 1mm; recall that the range of the data is 7mm for this particular path point (see Figure 5-5). The stem plot Figure 5-7 in represents each discrete height sample as a small blue circle. The continuous CPF is approximated via a PCHIP interpolation between the median of each set of discretized values, shown as a solid red line in Figure 5-7.

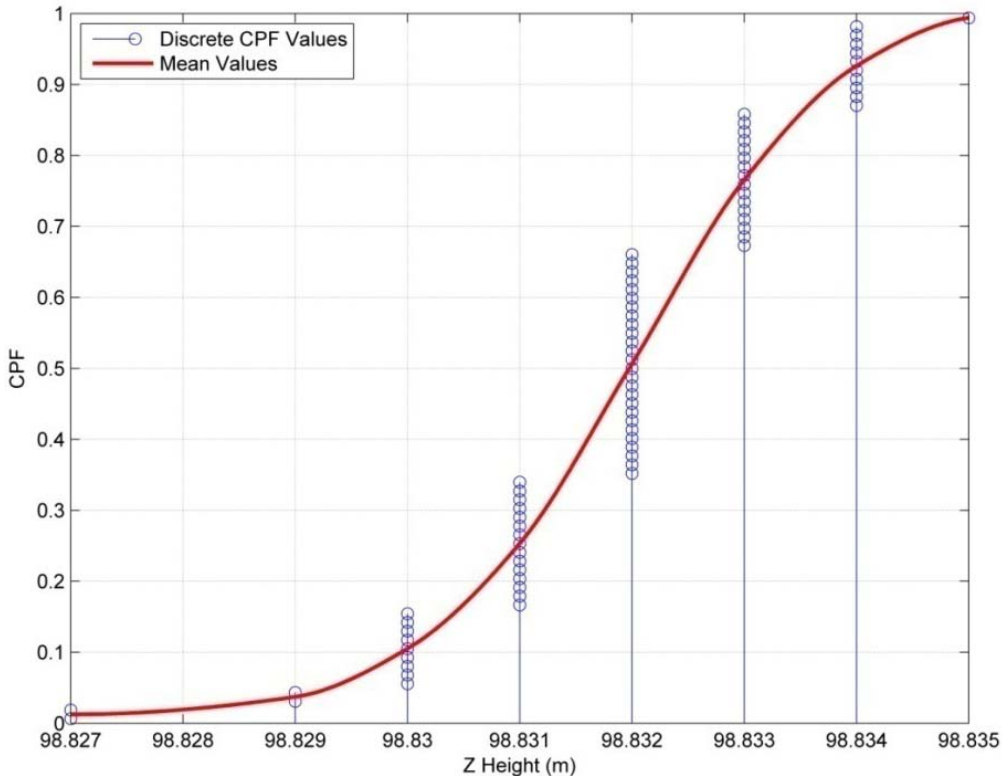

Figure 5-7: Discrete and Continuous Height Distributions

The techniques developed in this chapter propose to generate a 2D terrain profile using the information in the entire vehicle wheel path; however, more developmental work is required to prove that this method is genuinely superior to existing filters. Future work involves comparing the response of a physical vehicle to a vehicle model that is excited by 1) a simple 2D profile and 2) a 2D profile extracted from a 3D terrain surface.

The filtering technique developed in this work effectively maps 3D terrain surfaces to 2D terrain profiles, bridging the gap between simple 2D terrain measurement systems and more complex 3D surface measurement systems. This work proposes to select the median value of the CPF to represent the height at each path point; however, more complex stochastic methods are being pursued to better estimate these heights. This stochastic method selects a height at a particular path point by considering the gradient of the CPF at that point, and will improve the height estimation at that point.

5.4 Chapter 5 Conclusions

This chapter combines the best features of 2D terrain profiles and 3D terrain surfaces. The application of the method developed in this work results in a 2D terrain profile that emulates the mechanical filtering properties of a tire. The resulting terrain profile is extracted for any prescribed path in the horizontal plane. The method retains the topology information in the 3D surface that is required for the implementation of a tire model and effectively captures this information in the computational efficient 2D profile. That is, by building a CPF of accumulated height values at a particular path point, the general geometric characteristics of the surface remain in the extracted 2D profile. Additionally, these computationally efficient 2D terrain profiles will lead to better roughness estimates for pavement engineers, and the profiles will produce more precise estimates for virtual vehicle simulations. This increase in simulation fidelity will enable automotive engineers to improve vehicle designs at a fraction of the previous prototyping cost.

6. Conclusions

The techniques developed in this work address the needs of emerging terrain measurement applications. The specific novel contributions to terrain measurement developed in this work are:

1) A comprehensive accuracy test for high-fidelity terrain measurement systems
2) Two terrain-specific methods for attenuating inertial errors in terrain data.
3) A method to extract a 2D terrain profile from a 3D terrain surface that emulates a tire's mechanical filtering properties

Terrain measurement is an enabling technology to improve the vehicle modeling and simulation. Since the terrain surface is the primary source of excitation for the vehicle system, high-fidelity terrain measurements are critical for accurate simulations. Improving the fidelity of these measurements provides vehicle dynamicists information concerning wheel loads and system responses early in the design process; this pre-prototype knowledge allows design changes to be easily implemented and leads to superior vehicle designs.

References

1. Wambold, J.C., et al., *State of the Art of Measurement and Analysis of Road Roughness*. 1981: United States. p. 9p.

2. Karamihas, S.M., *Critical Profiler Accuracy Requirements*. 2005, University of Michigan Transportation Research Institute: Ann Arbor, Michigan. p. 130p.

3. Karamihas, S.M., *Development of cross correlation for objective comparison of profiles.* International Journal of Vehicle Design, 2004. **36**(2-3): p. 173-193.

4. Karamihas, S.M., *ACPA Profiler Repeatability Tests, 2005*. 2005: United States. p. 32p.

5. Sayers, M.W. and M.S. Karamihas, *The Little Book of Profiling*. 1998, The Regent of the University of Michigan: Ann Arbor, MI.

6. Kern, J.V. and J.B. Ferris. *Development of a 3D Vehicle-Terrain Measurement System Part I: Equipment Setup*. in *Proceedings of the Joint North America, Asia-Pacific ISTVS Conference*. 2007. Fairbanks.

7. Wagner, S.M., et al. *Development of a 3D Vehicle-Terrain Measurement System Part II: Signal Processing and Validation*. 2007. Fairbanks, Alaska: Proceedings of the Joint North America, Asia-Pacific ISTVS Conference and Annual Meeting of the Japanese Society for Terramechanics.

8. Herr, W.J., *Highway Profile Measuring System*. 1996: United States of America.

9. Liu, F., et al. *A Kalman-filter based multi-sensor terrain profile measurement system: Principle, implementation and validation*. 2008. Bellingham WA, WA 98227-0010, United States: SPIE.

10. Shoop, S.A., *Finite Element Modeling of Tire-Terrain Interaction*. 2001: United States. p. 69p.

11. Kern, J.V., et al. *Characterizing 2D road profiles using ARIMA modeling techniques*. 2007. Orlando, FL, United States: SPIE, Bellingham WA, WA 98227-0010, United States.

12. Wagner, S.M. and J.B. Ferris. *A polynomial chaos approach to ARIMA modeling and terrain characterization*. 2007. Bellingham WA, WA 98227-0010, United States: SPIE.

13. Wagner, S.M. and J.B. Ferris. *Reduced order ARIMA models of 2-D terrain profiles using singular value decomposition*. 2008. New York, NY 10016-5990, United States: American Society of Mechanical Engineers.

14. Ferris, J.B., *Factors affecting perceptions of ride quality in automobiles.* American Society of Mechanical Engineers, Dynamic Systems and Control Division (Publication) DSC, 1999. **67**: p. 649-654.

15. Kerchman, V., *Tire-suspension-chassis dynamics in rolling over obstacles for ride and harshness analysis.* Tire Science & Technology, 2008. **36**(3): p. 158-91.

16. Smith, H. and J.B. Ferris. *Post Processing Techniques to Correct Inertial Errors in High Fidelity Terrain Topology Measurements*. 2008. Turin, Italy: International Conference of the ISTVS.

17. Smith, H. and J.B. Ferris, *Mapping a 2D Profile from a 3D Terrain Surface by Emulating a Tire's Filtering Properties.* Submitted to the International Journal of Vehicle Systems Modelling and Testing, 2009.

18. Gillespie, T.D., M.W. Sayers, and L. Segel, *Calibration of Response-Type Road Roughness Measuring Systems*. 1980: United States. p. 91p.

19. Hveem, F.N., *Devices for Recording and Evaluating Pavement Roughness*. 1960, Highway Research Board Bulletin 264. p. 1-26.

20. Dembski, N., G. Rizzoni, and A. Soliman. *Development of a terrain severity measurement system utilizing optical lasers*. 2006. Bellingham WA, WA 98227-0010, United States: International Society for Optical Engineering.

21. Spangler, E.B. and W.J. Kelly, *GMR Road Profilometer-A Method for Measuring Road Profile.* 1966, Highway Research Board 121. p. 27-54.

22. Prem, H. *A Laser Based highway Speed Road Profile Measuring System*. 1987. Prague, Czechoslovakia: Proc. 10th International Association for Vehicle System Dynamics (IAVSD 1987).

23. Beres, W., *LINEAR MODELS OF TYRE ENVELOPING PROPERTIES.* International Journal of Vehicle Design, 1987. **8**(4-6): p. 485-503.

24. Smith, H. and J.B. Ferris. *Excitation Event Design and Accuracy Verification Procedure for High Fidelity Terrain Measurement Systems*. in *Submitted to the SPIE*. 2009. Orlando, FL.

25. Kennedy, S., J. Hamilton, and H. Martell. *Architecture and system performance of SPAN-NovAtel's GPS/INS solution*. 2006. Piscataway, NJ 08855-1331, United States: Institute of Electrical and Electronics Engineers Inc.

26. Herr, W.J., et al. *Continuous deflection basin measurement and backcalculation under a rolling wheel load using scanning laser technology*. 1995. New York, NY, USA: ASCE.

27. Herr, W.J. and W.G. Johnson. *Measurement of pavement deflection under a moving wheel utilizing scanning laser technology*. 1995. Bellingham, WA, USA: Society of Photo-Optical Instrumentation Engineers.

28. Perera, R.W., S.D. Kohn, and S. Bemanian, *Comparison of road profilers.* Transportation Research Record, 1996(1536): p. 117-124.

29. Vorburger, T.F., et al., *Calibration of Road Roughness Measuring Equipment. Volume 1. Experimental Investigation*. 1989: United States. p. 94p.

30. Vorburger, T.V., et al., *Calibration of Road Roughness Measuring Equipment. Volume 2. Calibration Procedures*. 1989: United States. p. 34p.

31. Hudson, W.R. and D.W. McKenzie, *DEPLOYMENT OF A DIGITAL ROAD PROFILOMETER*. 1983.

32. Queiroz, C.A.V. *CALIBRATING RESPONSE-TYPE ROUGHNESS MEASUREMENT SYSTEMS THROUGH ROD-AND-LEVEL PROFILES*. 1983. Washington, DC, USA: Transportation Research Board.

33. Mimuro, T., T. Maemura, and H. Fujii. *Development and Application of the Road Profile Measuring System*. 1992. Warrendale, PA: Society of Automotive Engineers, Inc.

34. Delanne, Y. and P.A.A. Pereira, *Advantages and Limits of Different Road Roughness Profile Signal-Processing Procedures Applied in Europe.* 2001: p. 254-259.

35. Sayers, M. *Development, Implementation, and Application of the Reference Quarter Car Simulation*. 1985. Bal Harbour, FL: ASTM.

36. Sayers, M.W., *On the calculation of international roughness index from longitudinal road profile.* Transportation Research Record, 1995(1501): p. 1-12.

37. Stone, R. and J.K. Ball, *Automotive Engineering Fundamentals*. 2004, Warrendale, PA: Society of Automotive Engineers, Inc.

38. Inman, D.J., *Engineering Vibration*. 2008, Upper Saddle River, NJ: Pearson Education, Inc.

39. Mueller, T., et al. *Identifying Vehicle Model Parameters using Measured Terrain Data*. 2009. Detroit, MI: Submitted to the SAE World Congress.

40. Ahlin, K., J. Granlund, and F. Lindstrom, *Comparing road profiles with vehicle perceived roughness.* International Journal of Vehicle Design, 2004. **35**(2-3): p. 270-86.

41. Walker, R.S. and E. Becker, *Collecting Stop and Go Inertial Profile Measurements*. 2006: United States. p. 56p.

42. Detweiler, Z.R. and J.B. Ferris. *Uniform Grid Spacing for Three Dimensional High Fidelity Terrain Profiles*. in *16th International Conference of the International Society for Terrain-Vehicle Systems*. 2008. Torino, Italy.

43. Ferris, J.B. *Capturing planer tire enveloping properties using static contraint modes*. 2006. New York, NY 10016-5990, United States: American Society of Mechanical Engineers.

44. Smith, H. and J.B. Ferris. *Post Processing Techniques to Correct Inertial Measurements in High Fidelity Terrain Topology Measurements*. 2008. Turin, Italy: International Conference of the ISTVS.

45. Vardeman, S.B. and J.M. Jobe, *Basic Engineering Data Collection and Analysis*. 2001, Pacific Grove: Duxbury.

Appendix

Table 1: Quarter Car Parameters

Parameter	Description
M_s	Sprung Mass
m_{us}	Unsprung Mass
k_s	Suspension Stiffness
c_s	Suspension Damping Coefficient
k_t	Tire Stiffness
$z_{s,us,t}$	Positive Coordinate Frame for Sprung Mass, Unsprung Mass, and Terrain

Table 2: Excitation Event Parameters

Parameter	Description
$L_{excitation}$	Excitation Event Length
a	Cleat Spacing
w	Cleat Width
V	Terrain Profiler Velocity
h	Cleat Height
x	Positive Horizontal Coordinate
z	Positive Vertical Coordinate
f_1	Primary Ride Frequency (Hz)
f_2	Wheel-Hop Frequency (Hz)
T	Displacement Transmissibility Ratio
r	Frequency Ratio
ζ_s	Damping Ratio
A	Amplitude of Vibration
t	Time